

Integrated High Temperature Coal-to-Hydrogen System with CO₂ Separation

Final Scientific Report

Reporting Period Start Date: 06/01/2005

Reporting Period End Date: 05/31/2007

Principal Authors: James A. Ruud, Anthony Ku, Vidya Ramaswamy, Wei Wei, and Patrick Willson

Date Report was Issued: August 2007

DOE Award Number: DE-FC26-05NT42451

Name and Address of Submitting Organization:

GE Global Research

1 Research Circle

Niskayuna, NY 12309

Disclaimer

“This report was prepared as an account of work sponsored by an agency of the United States Government. Neither the United States Government nor any agency thereof, nor any of their employees, makes any warranty, express or implied, or assumes any legal liability or responsibility for the accuracy, completeness, or usefulness of any information, apparatus, product, or process disclosed, or represents that its use would not infringe privately owned rights. Reference herein to any specific commercial product, process, or service by trade name, trademark, manufacture, or otherwise does not necessarily constitute or imply its endorsement, recommendation, or favoring by the United States Government or any agency thereof. The views and opinions of authors expressed herein do not necessarily state or reflect those of the United States Government or any agency thereof.”

ABSTRACT

A significant barrier to the commercialization of coal-to-hydrogen technologies is high capital cost. The purity requirements for H₂ fuels are generally met by using a series of unit clean-up operations for residual CO removal, sulfur removal, CO₂ removal and final gas polishing to achieve pure H₂. A substantial reduction in cost can be attained by reducing the number of process operations for H₂ cleanup, and process efficiency can be increased by conducting syngas cleanup at higher temperatures.

The objective of this program was to develop the scientific basis for a single high-temperature syngas-cleanup module to produce a pure stream of H₂ from a coal-based system. The approach was to evaluate the feasibility of a “one box” process that combines a shift reactor with a high-temperature CO₂-selective membrane to convert CO to CO₂, remove sulfur compounds, and remove CO₂ in a simple, compact, fully integrated system.

A system-level design was produced for a shift reactor that incorporates a high-temperature membrane. The membrane performance targets were determined. System level benefits were evaluated for a coal-to-hydrogen system that would incorporate membranes with properties that would meet the performance targets.

The scientific basis for high temperature CO₂-selective membranes was evaluated by developing and validating a model for high temperature surface flow membranes. Synthesis approaches were pursued for producing membranes that integrated control of pore size with materials adsorption properties. Room temperature reverse-selectivity for CO₂ was observed and performance at higher temperatures was evaluated. Implications for future membrane development are discussed.

TABLE OF CONTENTS

Disclaimer.....	2
Abstract.....	3
Executive Summary.....	5
1 System design.....	7
1.1 Introduction.....	7
1.2 Membrane reactor design.....	9
1.3 System performance.....	14
1.4 Conclusions.....	16
2 High temperature CO ₂ membrane materials.....	17
2.1 Membrane design.....	17
2.2 Synthesis of mesoporous inorganic membrane structures.....	21
2.2.1 Experimental methods.....	21
2.2.2 Defect rate measurement.....	24
2.2.3 Process development for silica membranes.....	25
2.2.4 Room temperature separation measurements.....	31
2.3 Model for high temperature membrane performance.....	35
2.3.1 Adsorption measurements.....	35
2.3.2 Membrane measurements.....	38
2.4 Materials selection.....	45
2.5 Synthesis of functionalized mesoporous membranes.....	50
2.6 Synthesis of barium titanate based membranes.....	54
2.7 Conclusions.....	57
References.....	59
List of figures.....	61
List of tables.....	64
List of acronyms and abbreviations.....	65

EXECUTIVE SUMMARY

A significant barrier to the commercialization of coal-to-hydrogen technologies is high capital cost. The purity requirements for H₂ fuels are generally met by using a series of unit clean-up operations for residual CO removal, sulfur removal, CO₂ removal and final gas polishing to achieve pure H₂. A substantial reduction in cost can be attained by reducing the number of process operations for H₂ cleanup, and process efficiency can be increased by conducting syngas cleanup at higher temperatures.

The objective of this program was to develop the scientific basis for a single high-temperature syngas-cleanup module to produce a pure stream of H₂ from a coal-based system. The approach was to evaluate the feasibility of a “one box” process that combines a shift reactor with a high-temperature CO₂-selective membrane to convert CO to CO₂, remove sulfur compounds, and remove CO₂ in a simple, compact, fully integrated system.

A system-level design was produced for a shift reactor that incorporates a high-temperature membrane. The design features a multi-train, counter-current membrane reactor. Syngas and sweep streams enter the reactor from opposite ends and are divided into 8 tubular membrane reactor module trains. Each module contains membrane tubes where syngas and steam flow in a counter-current direction on the two sides of each tube. The key design parameters and their target values were determined, including the membrane selectivity, membrane permeability, functional layer thickness, pressure differential, CO₂ capture fraction, tube length, tube inner diameters, and tube number.

The system using the CO₂ membrane reactor can attain overall system efficiency benefits greater than 2% over than the base case. The efficiency improvement of using a CO₂ membrane reactor in a coal-to-hydrogen plant comes primarily from the following sources:

- The CO₂ membrane WGS reactor requires less high pressure steam in the syngas.
- The higher cleanup temperature avoids the heat up and cool down associated with conventional low temperature cleanup processes.

On the other hand, the primary sources of efficiency loss of a CO₂ membrane reactor include:

- H₂ loss through the membrane
- The power consumption of CO₂ compression.

The elimination of multiple unit operations (low temperature gas cooling, sulfur removal, solvent regeneration, and CO₂ removal) and the consolidation of WGS reactor, sulfur removal, and CO₂ capture into an integrated module reduced capital costs. There is a reduction in the plant footprint for the clean-up section by a factor of at least two. This capital expenditures analysis indicates a potential of up to 3% CAPEX savings for a coal-to-hydrogen plant by using the proposed one-box module over conventional syngas cleanup system.

A scientific basis for the high temperature CO₂-selective membranes required to enable the “one box” system was developed. A quantitative model was produced and validated for the design of membrane materials capable of high temperature CO₂ reverse selectivity. The model describes porous membranes in which selectivity is endowed through the mechanism of preferential adsorption and surface diffusion of CO₂ along the pore walls. Selectivity for CO₂ over H₂ requires that the surface flow of CO₂ is large compared with the Knudsen flow of H₂ through the

bulk of the pore. Selectivity can result from the combination of two mechanisms: enhanced CO₂ surface transport and hindered H₂ transport. Three key membrane design parameters were identified: surface concentration of CO₂, heat of adsorption of CO₂ and effective pore radius. The first two parameters are intrinsic materials parameters that describe the rate of surface diffusion of CO₂. They were measured from chemisorption measurements on oxide powders. The third parameter is a microstructural parameter which accounts for the competitive Knudsen flux of H₂ and for the extent of hindered H₂ flux from pore blocking.

Silica membranes were developed that were free of viscous defects and which had an effective pore radius of less than 1 nm. Those membranes showed reverse selectivity for CO₂/H₂ at room temperature. The selectivity decreased with increasing temperature due to the decrease in surface concentration of CO₂. That caused two effects: the surface transport rate for CO₂ decreased and the H₂ Knudsen flow rate increased as the effective pore size increased. Good quantitative validation was obtained for the predicted selectivity with temperature using the measured chemisorption parameters and only one fitting parameter for the effective pore radius.

On the basis of the model, membrane design parameters were established for the membrane parameters that would allow the attainment of system level separation targets. For pore size diameters of 1-2 nm, heat of adsorption of less than 25 kJ/mol and CO₂ surface concentration greater than 2 μmol/cm² are required. Materials were screened based on measured and literature adsorption isotherms, with three materials identified as promising candidates.

Two approaches were pursued to synthesize membranes with both the required effective pore size and CO₂ adsorption characteristics. First, silica membranes with the required pore size were functionalized with alkaline and rare earth oxides in order to increase the surface adsorption of CO₂. Second, synthesis of barium-titanate-based membranes was pursued in order to obtain the required pore size in a material determined to have the required CO₂ surface affinity.

The functionalized silica membranes were produced without viscous defects but no increase in the high temperature CO₂ reverse selectivity over the baseline materials was observed. That may have been due to an inhomogeneous distribution of the functional groups within the membrane or due to a limitation in the concentration attained.

A series of barium-titanate-based membranes was produced that were free of viscous defects, but high temperature reverse selectivity was not observed. For the membrane processing temperatures required to produce pure barium titanate, the effective pore size was too large to observe reverse selectivity. At lower processing temperatures, there was a barium carbonate phase present. Only a small increase in CO₂ selectivity over the Knudsen value at room temperature was observed.

Future work for developing reverse-selective CO₂ membranes should focus on developing new processing methods for control of pore size in the materials identified by modeling to be promising candidates. In addition, the materials screening methodology can be applied to identify additional materials that are more amenable to membrane processing in the desired pore size range.

1 SYSTEM DESIGN

1.1 INTRODUCTION

A CO₂ selective water-gas-shift (WGS) membrane reactor design was identified as a candidate design for the high temperature integrated syngas cleanup system with CO₂ separation. This reactor design concept is characterized by a reactor containing hollow membrane ceramic fibers, sulfur-tolerant WGS catalyst and a sweep gas system. Preliminary cost analysis for the design concept was carried out to determine the economic benefits as well as the capital cost sensitivities of various system parameters. These in turn were used to identify the preliminary performance targets for the membrane material development. To understand the impact of the membrane reactor concept on the system efficiency, a base case coal-to-hydrogen system analysis model was constructed using Aspen Plus software. Based on the baseline model, the process model for the coal-to-hydrogen using integrated CO₂ membrane reactor was built using a customized membrane reactor module. The preliminary analysis results indicate that the a coal-to-hydrogen system with integrated CO₂ membrane reactor has a lower capital cost as well as a higher system efficiency compared with a conventional coal-to-hydrogen plant. Based on the analyses, the key components of the optimal membrane reactor design were down-selected and the membrane material performance targets identified.

The conceptual design of the integrated high-temperature membrane reactor was identified based on the conventional coal-to-hydrogen plant process requirements, and it leveraged existing membrane reactor designs for other reaction processes obtained from the literature. The goal was to obtain benefits of process intensification from the integration of several syngas clean-up steps into a single reactor. According to the process flow diagram of a typical coal-to-hydrogen plant with CO₂ removal (as shown in Figure 1)[Gray, 2002], [Chiesa, 2005], the features of the CO₂ membrane reactor for processes intensification were identified as:

- An integrated high temperature WGS reactor
- Selective removal of CO₂
- Selective removal of H₂S

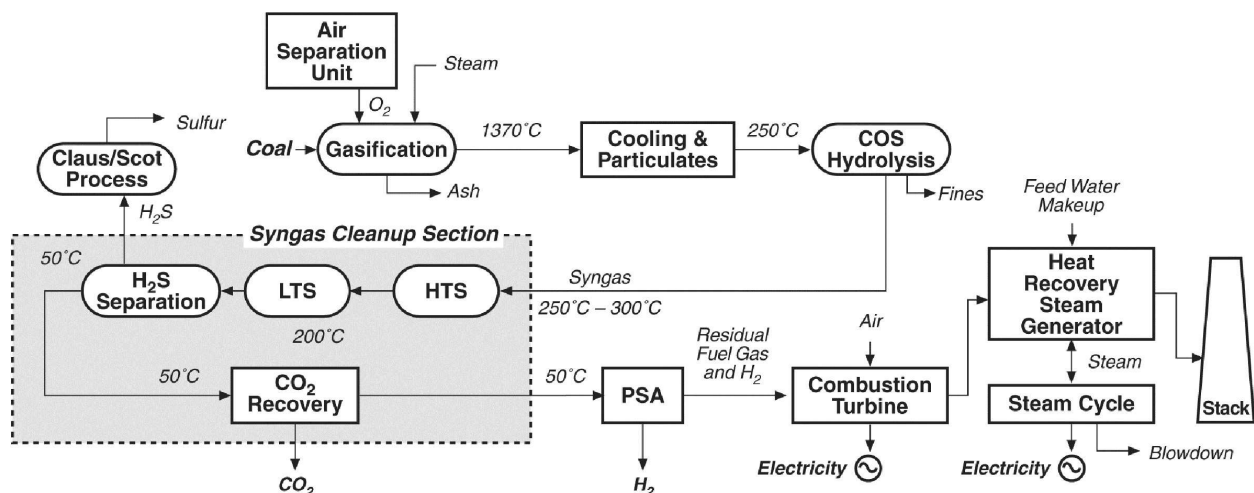


Figure 1-1. Process flow diagram of coal-to-hydrogen plant with CO₂ separation

A wide literature survey was also conducted, which focused on various membrane reactor designs including concurrent flow, countercurrent flow, cross flow, hollow fiber, tubular, plate, and other configurations. The preliminary membrane design concept was selected based on the engineering calculations and the critical performance characteristics of the system.

Figure 1-2 shows the conceptual design of the water gas shift (WGS) membrane reactor in a integrated gasification combined cycle (IGCC) coal-to-hydrogen plant with CO₂ separation. The membrane reactor uses hollow fiber ceramic membranes, sulfur-tolerant WGS catalyst and a sweep gas system. One configuration of the integrated membrane reactor incorporates the WGS catalyst within the hollow CO₂-selective membrane fiber tubes. The syngas flow is directed within the membrane fiber tubes where it undergoes the WGS reaction while the membrane selectively removes CO₂ from the reaction into the sweep gas stream on the exterior of the membrane tube. The continuous removal of CO₂, therefore, shifts the WGS reaction equilibrium to nearly 100% CO conversion. At the outlet of the membrane tubes, a hydrogen purity of over 90% can be achieved. On the other hand, CO₂ is captured in the counter-current sweep stream (low quality steam) at pressure and can be easily sequestered for geological storage or enhanced oil recovery. A section of the membrane for H₂S removal can be placed before or after the CO₂ removal segment. Other configurations of the hollow membrane fiber tube design may include syngas and WGS catalyst on the shell side of the membrane tube with the sweep gas flow through the inside of the tubes. Therefore the membrane reactor design integrates multiple functions, including WGS, hydrogen separation, CO₂ separation and acid gas removal, in one reactor module.

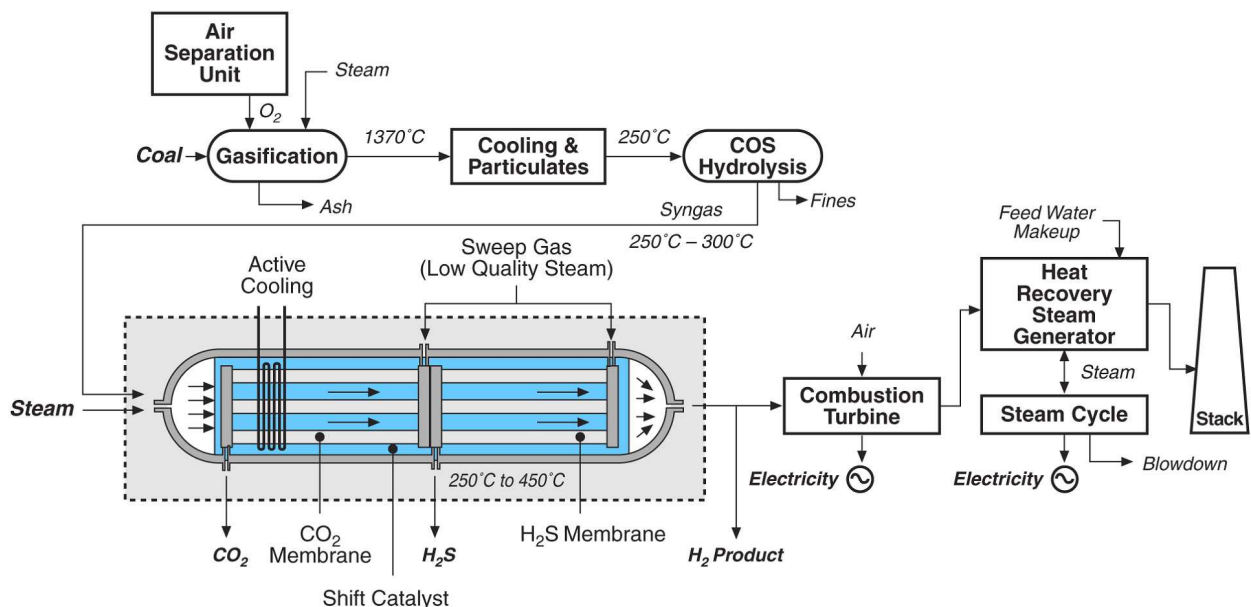


Figure 1-2. CO₂-selective WGS membrane reactor in a coal-to-hydrogen plant

1.2 MEMBRANE REACTOR DESIGN

To identify the detailed component design of the integrated membrane reactor, the following critical design features and requirements were identified:

- The integrated membrane reactor should satisfy the basic function as a syngas cleanup unit where the removal of CO₂ is accomplished by membrane separation.
- From a practical point of view, the reactor unit and its components should be easy to fabricate, reliable to operate and easy to maintain.
- The integrated reactor should have a relatively low capital cost comparing to current syngas cleanup and CO₂ separation equipments.
- The integrated membrane reactor should also have low energy consumption in terms of heating and cooling and steam usage.

The prototype reactor features a multi-train, counter-current membrane reactor design as shown in Fig 1-3. Syngas and sweep streams enter the reactor from opposite ends and are divided into 8 tubular membrane reactor module trains. Each module contains membrane tubes where syngas and steam flow in a counter-current direction on the two sides of each tube. The prototype reactor was sized to the syngas flow from a 100MW IGCC plant. The key design parameters and their target values were determined, including the membrane permeability, functional layer thickness, pressure differential, CO₂ capture fraction, tube length, tube inner diameters, and tube number.

In comparison with a single-train design, the multi-train reactor can provide a more uniform distribution of shell-side gas streams within the reactor module. More importantly, this design produces membrane modules with individual parts counts selected to facilitate mass manufacturing. In case of maintenance or membrane failure, the multi-train design can isolate faulty component from remaining modules and therefore provides benefits from a reliability, availability and maintainability point of view.

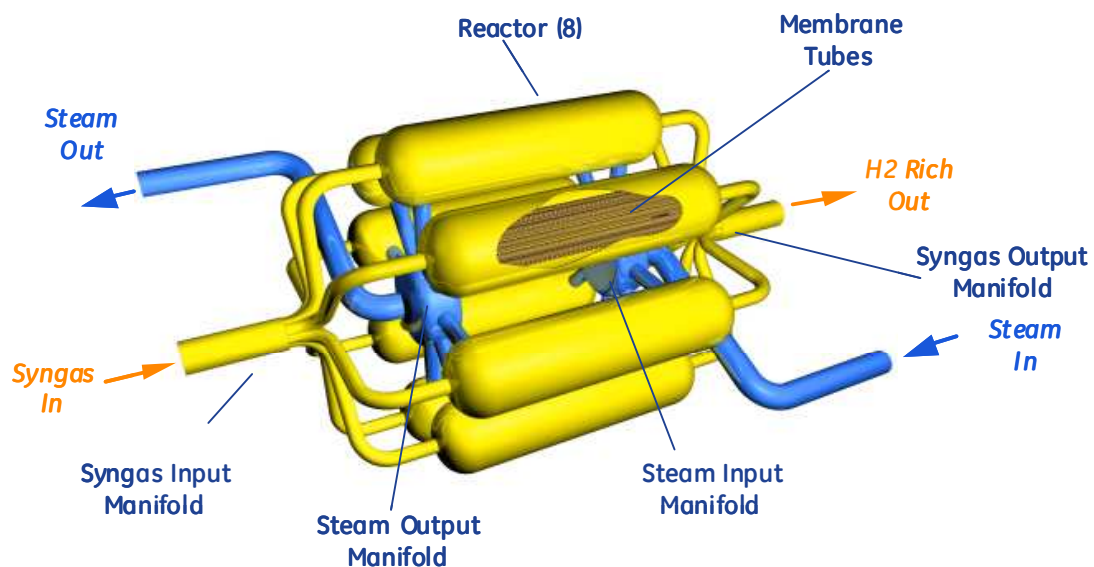


Figure 1-3. Prototype membrane reactor design

The reactor prototype design was developed into a fully integrated detailed reactor model. The model accounts for mass balance on both the permeate side and retentate side of the membrane, heat transfer across the membrane walls and detailed WGS kinetic model to calculate the reaction rate, conversion and adiabatic heat release during the reaction. The membrane reactor model was validated against similar reactor models [Huang, 2005]. The WGS kinetics is fairly well known and an iron-based catalyst was assumed for the kinetic model in this study.

The counter-current membrane reactor model for the prototype membrane reactor design, shown in Figure 1-4, was developed using Aspen Custom Modeler software and was integrated in AspenPlus software for overall plant efficiency analysis. This reactor model was based on a prior system analysis study where a set of membrane performance targets was identified to meet the project goals in terms of efficiency and economic benefits.

To provide a consistent basis for benchmarking, a two-stage WGS reactor model was also developed as the baseline case. The two models, as shown in Figure 1-4, were both developed in Aspen Custom Modeler and were based on the same set of operation conditions and comparable assumptions. The base case two-stage WGS reactor model has a high temperature shift (HTS) segment and a low temperature shift (LTS) segment. Its underlying kinetic parameters were validated by comparison with published literature data. The model can accurately predict the spatial profiles of the syngas composition and temperature along the reactor, taking into account the inlet syngas composition (including the steam-to-CO ratio), the inlet temperature and pressure, the residence time and catalyst loading. The countercurrent membrane reactor model was constructed using the same kinetic models validated in the baseline case without any modifications.

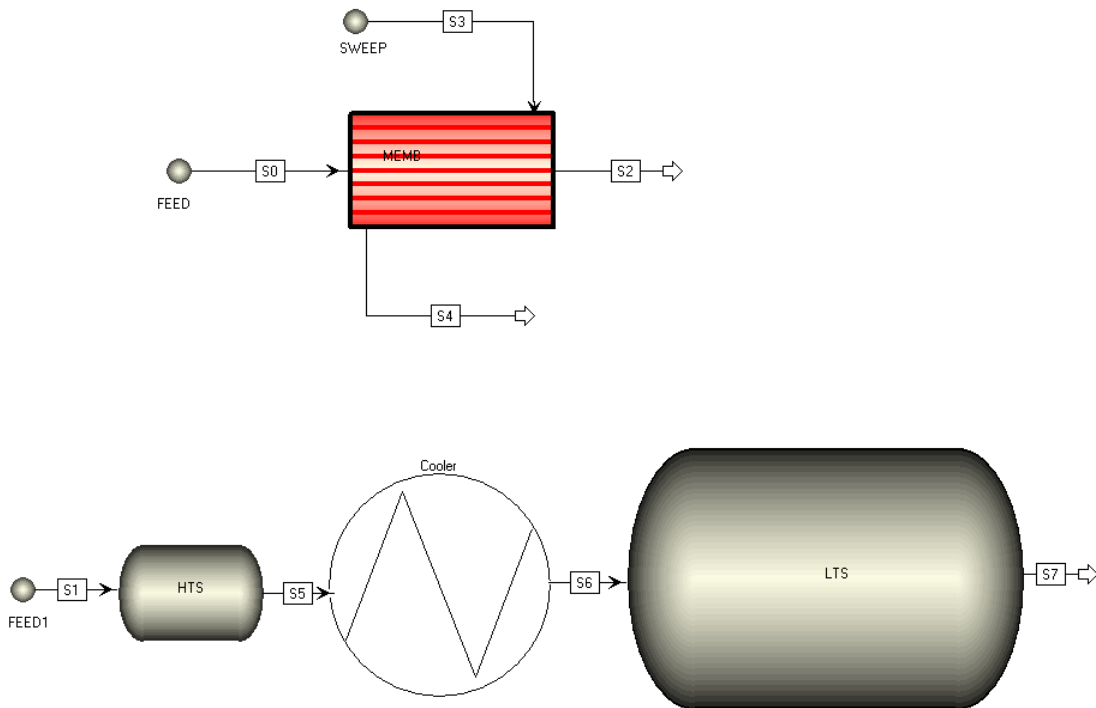


Figure 1-4. Membrane reactor model and baseline case two-stage water gas shift model.

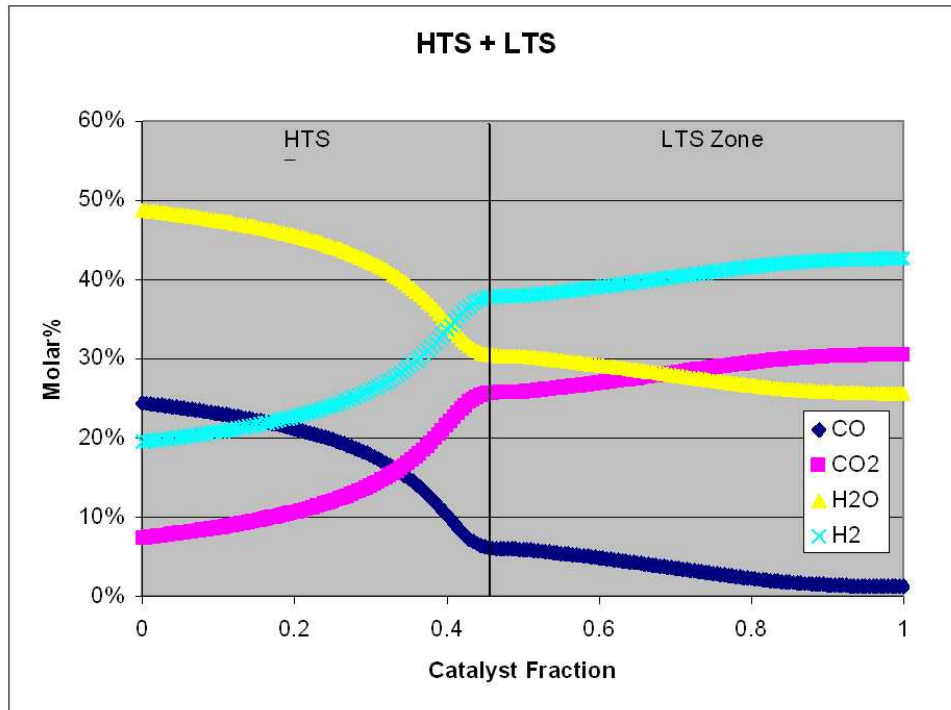


Figure 1-5. Gas composition profile in a two-stage water-gas-shift reactor

The detailed countercurrent membrane reactor model simulates an eight parallel train design, with multiple ceramic hollow membrane tubes in each train where the syngas and steam are flowing counter-currently on the two sides of each ceramic tube. An example of the results of the heat and mass transfer analysis for the two-stage WGS reactor is shown in Figure 1-5. The WGS reaction rate for the conversion of CO to H₂ and CO₂ is fairly rapid in the HTS zone. The reaction rate increases along the length of the reactor as the exothermic heat of the reaction raises the reactor temperature to above 450 °C. At that temperature, however, the WGS reaction reaches equilibrium, and the reaction stops. At that point, typically only 75% of the CO is converted. The syngas mixture must be cooled to about 200 °C in a heat exchanger before entering the LTS zone. The reaction rate and temperature rise in the LTS zone is slower due to the low temperature. At the end of the two-stage WGS reactor, the majority of the remaining 25% of the CO is converted into H₂ and CO₂ with an effective overall CO conversion of above 95%.

For comparison, an example of a heat and mass transfer analysis for the CO₂ membrane WGS reactor is shown in Figure 1-6. The membrane properties were CO₂/H₂ selectivity of 60 with a permeance of 6.7×10^{-7} mol/m²-s-Pa. The reaction rate is high at the entrance of the reactor, and it increases with a substantial temperature rise in the initial section of the reaction bed. However, unlike the conventional WGS reactor, the membrane reactor continuously removes CO₂ from the syngas stream into the sweep gas stream through the membrane. That shifts the reaction equilibrium towards more CO conversion and more hydrogen production. At the same time, the sweep gas on the other side of the membrane hollow tube acts to moderate the temperature rise

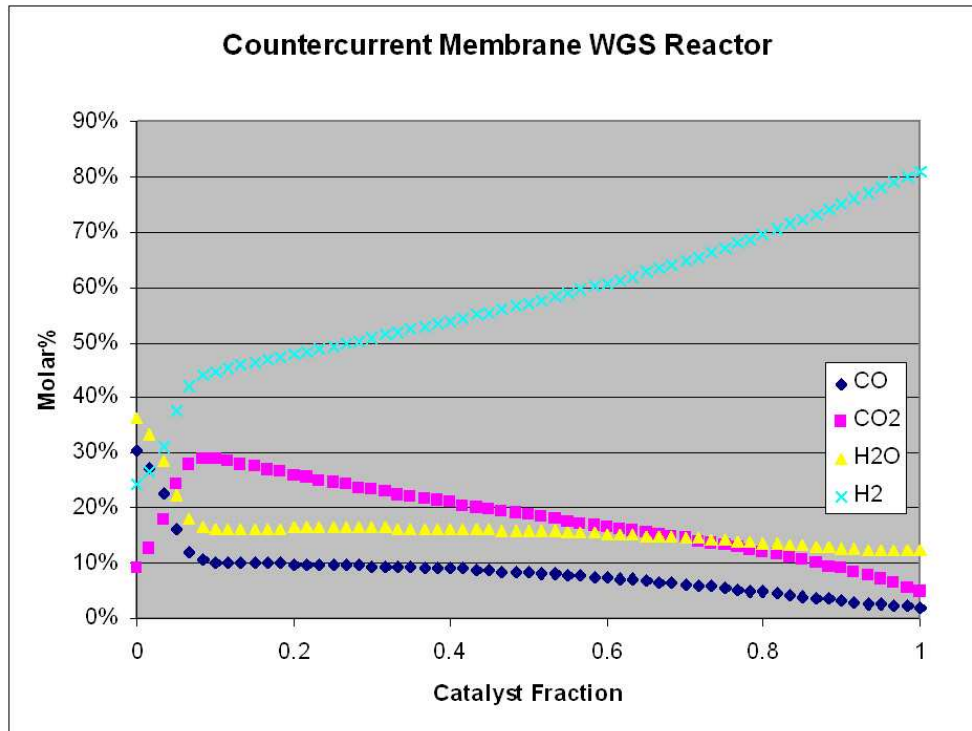


Figure 1-6. Gas composition profile in a CO₂ membrane water-gas-shift reactor.

from the exothermic reaction. That results in an ideal temperature profile parallel to the chemical equilibrium and maintains a constant driving force for the forward WGS reaction. Together, the integrated membrane reactor can achieve same level of CO conversion as the conventional two-stage system, while requiring about 36% less catalyst.

One of the key differences between the two reactors is the steam-to-CO-ratio requirement. Conventional two-stage WGS reactors typically require a steam-to-CO-ratio of over 2:1. The excess steam shifts the reaction equilibrium toward more H₂ production, and it also serves to moderate the local catalyst temperature to prevent coking. In a countercurrent membrane reactor, however, the constant removal of CO₂ via the membrane provides a continuous shift of equilibrium towards hydrogen production, thus eliminating the need for additional steam injection. Furthermore, the countercurrent membrane reactor can utilize waste heat from steam cycle, which functions as a catalyst temperature controller to avoid catalyst coking. As a result, the membrane reactor requires only a stoichiometric steam-to-CO ratio (1:1), while a conventional two-stage WGS reactor requires additional high-pressure injection to achieve steam-to-CO ratio of at least two. This difference in the high pressure steam requirement is tied directly to the overall system efficiency performance, which will be discussed in subsequent section.

The detailed reactor models not only enable the optimization of the membrane reactor design, but also provide important information on the operation condition, reaction rates and separation ratio required by the overall system analysis models to produce accurate predictions of the overall system efficiency performance and even capital cost estimates in a coal to hydrogen plant.

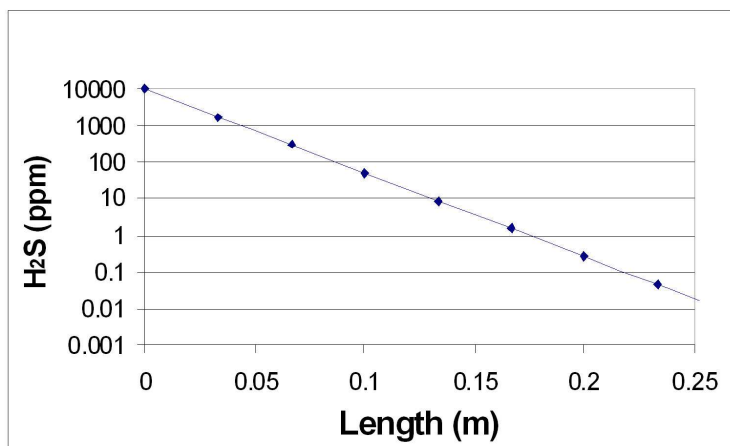


Figure 1-7. H₂S composition profile in a CO₂-membrane water-gas-shift reactor.

A similar analysis was performed for H₂S removal through the membrane. The membrane was assumed to have a selectivity of H₂S/H₂ of 8000 and a permeance of 6.7×10^{-7} mol/m²-s-Pa. The gas composition profile for H₂S is given in Figure 1-7. H₂S levels were below 1 ppm at 1/10th of the length of the reactor required for the CO₂ removal. However, the required selectivity of the membrane for H₂S was much higher than that for CO₂.

Heat and mass transfer models were produced for the baseline case two-stage WGS reactor as well as the CO₂-membrane reactor being developed on this program. The models were validated with the literature. Gas composition and thermal profiles were evaluated as a function of position in the reactor. The models can be integrated in a system level ASPEN model to evaluate impact on system performance of a coal-to-hydrogen system. It was determined that the CO₂ membrane reactor requires significantly less steam and catalyst amount than the two-stage reactor to attain the same level of CO conversion.

1.3 SYSTEM PERFORMANCE

A series of detailed system studies were conducted to identify the potential energy and cost savings of replacing the conventional syngas cleanup system with an integrated CO₂-selective membrane WGS reactor.

The baseline case was a coal-to-hydrogen system using a conventional syngas cleanup system. Illinois #6 coal was used with a pressurized, single-stage, slurry fed, oxygen blown gasifier. A water quench reduced the syngas temperature and removed particulates and water soluble impurities. A COS hydrolysis stage converted sulfur compounds to H₂S. The cleanup section consisted of a two-stage WGS reactor, gas cooling, Selexol sulfur and CO₂ removal and a pressure swing adsorption (PSA) stage for H₂ purification. The tailgas of the PSA was sent to a waste heat boiler system including a heat recovery steam generator and a steam turbine. The H₂S was sent to a Claus/Scot process. The CO₂ was compressed to 2000 psi and the H₂ was purified to greater than 99.999% and pressurized to 450 psi. The baseline case was similar to one analyzed in the literature [Gray, 2002].

Several system configurations using a CO₂-membrane WGS reactor in place of the two-stage WGS reactor and the Selexol process were evaluated. The system included a high-pressure gasifier with water quench and COS hydrolysis. The syngas was fed into a CO₂-membrane WGS reactor described by the detailed model. Low pressure steam was used as a sweep gas to remove CO₂. The residual H₂ in the sweep gas was utilized to heat the gas temperature before being sent to a heat recovery steam generator and a CO₂ compressor. The H₂ exiting the reactor was split into two streams for polygeneration of H₂ and electricity. The H₂ product stream was further purified with a small-scale pressure swing adsorber. The H₂ stream for electricity production was sent to a combined cycle gas turbine. The membrane requirements were given in section 1.2.

For each of the cases analyzed in the study, an AspenPlus system simulation was constructed, corresponding to a 3000 TPD bituminous coal based gasification plant. 90% CO₂ capture was achieved. The gasification system conditions for the coal-to-hydrogen production systems were based on those from literature references [Gray, 2002], [Chiesa, 2005]. An example of a result from the system study is given in Table 1-1.

Table 1-1. Calculated system parameters

	Baseline Case	CO ₂ Membrane Reactor
Total gross power (MW)	72	89
Steam turbine power (MW)	72	58
Gas turbine power (MW)	0	31
Auxiliary power load (MW)	55	73
Net power (MW)	17	16
H ₂ production (L/min) (MMscfd)	2.34x10 ⁶ (119)	2.47x10 ⁶ (125.6)
Efficiency (% HHV)	59.9	62.8

The system using the CO₂ membrane reactor can attain overall system efficiency benefits as high as about 2.9% over than the base case. The efficiency improvement of using a CO₂ membrane reactor in a coal-to-hydrogen plant comes primarily from the following sources:

- The CO₂ membrane WGS reactor requires less high pressure steam in the syngas, leading to about 2% overall system efficiency improvement.
- The CO₂ membrane reactor cleanup system avoids the need of steam as stripping gas in a Selexol process.
- The bulk H₂ stream after the membrane reactor is at relatively high pressure and high purity, >90%, which can significantly reduce overall H₂ loss in the PSA process.
- The higher cleanup temperature avoids the heat up and cool down associated with conventional low temperature cleanup processes.

On the other hand, the primary sources of efficiency loss of a CO₂ membrane reactor include:

- H₂ loss through the membrane
- The power consumption of CO₂ compression.

A high-level capital cost analysis was performed for a coal-to-hydrogen plant using a membrane reactor compared with a baseline plant configuration that uses conventional syngas cleanup units. The costs for the baseline case were taken from published reports [Gray, 2002],[NETL, 2000],[Kreuz, 2005].

The following assumptions were used in the analysis of the cost of the system with the one-box cleanup reactor.

- The capital expenditures for similar components were assumed to be the same for both cases.
- The one-box system eliminates the cost of the base case equipment costs for low temperature gas cooling, sulfur removal, and CO₂ separation.
- The one-box system uses equipment for Claus and SCOT processes to recover sulfur from H₂S in the membrane sweep gas.
- The one-box system uses a small-scale pressure swing absorption (PSA) system for producing ultra-high-purity H₂. However, the unit cost is reduced in half because the one-box system delivers a pre-purified stream of H₂.
- The cost of the one-box unit is the cost of a conventional WGS reactor plus membrane material costs.
- The CO₂ and H₂S membrane segments meet the targets indicated in Section 1.2.
- The membrane cost is \$500/m².

The elimination of multiple unit operations (low temperature gas cooling, sulfur removal, solvent regeneration, and CO₂ removal) and the consolidation of WGS reactor, sulfur removal, and CO₂ capture into an integrated module reduced capital costs. There is a reduction in the plant footprint for the clean-up section by a factor of at least two. This capital expenditures (CAPEX) analysis indicates a potential of up to 3% CAPEX savings for a coal-to-hydrogen plant by using the proposed one-box module over conventional syngas cleanup system.

1.4 CONCLUSIONS

Several system case studies were evaluated. Results suggest that a CO₂ membrane reactor can be used to increase the efficiency, reduce the footprint and reduce the CAPEX of a coal-to-hydrogen system. A multi-train, counter-current, hollow tube membrane reactor module design was produced and membrane performance targets were established. For CO₂ separation, the membrane properties were CO₂/H₂ selectivity of 60 with a permeance of 6.7×10^{-7} mol/m²-s-Pa. The key technology challenge to the realization of the system is the feasibility of high temperature membrane materials, as described in the next section.

2 HIGH TEMPERATURE CO₂ MEMBRANE MATERIALS

2.1 MEMBRANE DESIGN

There are three types of transport for gas molecules through microporous membranes at elevated temperatures: Knudsen diffusion, molecular sieving, and surface diffusion [Shekawat, 2003]. Both Knudsen diffusion and molecular sieving result in higher transport rates for H₂ than CO₂ because H₂ is a lighter and smaller molecule than CO₂. To achieve selective separation of CO₂ from H₂ in a microporous membrane, surface diffusion must be the dominant mode of CO₂ transport. High selectivities require that the flux of CO₂ along the surface of the pores is much greater than the transport of H₂ through the interior of the pores.

The important parameters in the design of the reverse-selective CO₂ membrane are the pore size and the surface diffusion rate. Pore size must be large enough to permit the access of CO₂ to the pore surface to avoid the molecular sieving of H₂. However, it must be small enough to minimize the Knudsen diffusion of H₂ relative to the surface flux of CO₂.

There is evidence for selective surface transport of gases in inorganic membranes. Carbon membranes have shown been used to separate hydrogen from hydrocarbons [Rao, 1993], [Rao, 1996]. Surface transport of hydrogen sulfide and sulfur dioxide has been observed in alumina membranes up to 275 °C [Sloot, 1992]. Moon, et al. [Moon, 2004] have observed reverse-selectivity of CO₂ relative to H₂ in silica membranes at 40 °C with a separation factor as high as 7. They attributed the preferential transport of CO₂ to H₂ both to CO₂ surface diffusion and a reduction in H₂ transport through the pores due to the adsorbed CO₂ molecules (pore blocking). In those membranes, permeability of H₂ as a single gas was much higher than that for CO₂, but the effect of pore blocking in the separation of the gas mixture was required for the observation of reverse selectivity. However, there is little known evidence for high temperature surface transport membranes for CO₂ relative to H₂. [Bredesen, 2004].

The rate of surface diffusion of a gas molecule on a material surface is dependent on the heat of adsorption and the surface concentration gradient [Gilliland, 1974], [Horiuchi, 1998b]. A material with a high surface diffusion rate will have a low heat of adsorption and a high surface concentration for CO₂. Furthermore, for reverse selectivity it must be non-adsorbing for H₂. The amount of gas adsorbed on a surface typically increases with pressure and decreases with increasing temperature. Therefore to maintain a high selectivity at elevated temperatures, materials with high surface concentrations at temperature are required [de Lange, 1995].

Development of high temperature, reverse selective membranes can be aided by modeling the separation mechanisms in the membrane structure. Requirements for the critical pore size and the material adsorption properties can be derived to guide the synthesis efforts. Models of the gas flux through microporous membranes including surface diffusion have been developed [Keizer, 1988], [Moon, 2004]. However, explicit verification of the temperature dependence of the surface flow is not available, and there are no known treatments of the effect of pore blocking.

A model was developed and verified for the temperature dependence of CO₂/H₂ selectivity in microporous membranes. Silica was used as a model system to verify the model. Heat of adsorption and surface concentration were obtained from CO₂ adsorption measurements. The effective pore radius was the single fitting parameter which had a temperature dependence due to the effect of pore blocking.

Assuming a membrane is an ensemble of similar pores, it is useful to consider the different gas transport mechanisms through an average pore of radius r and length L , at temperature T and with a differential partial pressure ΔP between the pore inlet and exit. If r is much smaller than the mean free path of the gas molecule, the gas phase flow through the pore, in units of mols/time, by Knudsen diffusion is

$$Q_{Kn} = \frac{2r^3 \Delta P}{3L} \sqrt{\frac{8\pi}{MRT}} \quad (2-1)$$

The various molecular species in the feed stream will diffuse independently through the pore, with relative rates determined by the molecular weight and partial pressure difference of each gas. For equimolar mixtures, the flow of each gas is proportional to $1/\sqrt{M}$. Knudsen flow increases with increase in pore radius, and decreases with increasing temperature.

If one of the molecular species in the feed stream has an affinity for the pore wall surface, this species will tend to adsorb on the pore wall. Typically, the amount of adsorption will be proportional to the partial pressure of the molecule, and there will be a higher surface concentration of adsorbed molecules at the pore inlet. If the partial pressure at the outlet is lower, there will a gradient in surface concentration along the pore length. The steady state surface diffusive flux of the condensed species, in units of mols/length-time is given by

$$J_{surf} = -D \frac{dc}{dx}, \quad (2-2)$$

where D is the surface diffusivity of the molecule, c is surface concentration, and x is the distance along the pore length. The surface concentration profile $c(x)$, obtained by solving the steady state diffusion equation for the boundary conditions $c(0) = c_0$ at the inlet and $c(L) = c_L$ at the pore exit, yields a linear concentration profile,

$$c(x) = c_0 + \frac{x}{L}(c_L - c_0), \text{ and surface flux, } J_{surf} = -D \frac{c_0 - c_L}{L}. \quad (2-3)$$

The surface flow through the pore is equal to

$$Q_{surf} = -2\pi r D \frac{dc}{dx} = -2\pi r D \frac{c_0 - c_L}{L}. \quad (2-4)$$

In the above analysis, D is assumed to be concentration independent, while in general, D may be a function of concentration. Diffusivity can be expressed in the Arrhenius form,

$D = D_0 \exp(\frac{-q}{RT})$, where q is the activation barrier for surface hopping. Substituting for D , the surface flow can be expressed as

$$Q_{surf} = -2\pi r D_0 \exp(\frac{-q}{RT}) \frac{c_0 - c_L}{L}. \quad (2-5)$$

While Knudsen flow depends only on the physical dimensions of the pore, surface flow depends strongly on pore wall chemistry, since both surface concentration of the adsorbed gas and diffusivity are determined by the interaction of the gas molecule with the surface.

H₂ transport through SiO₂ membranes takes place entirely by Knudsen diffusion, since the H₂ adsorption on SiO₂ is negligible [de Lange, 1995]. However, CO₂ transport is attributed to both Knudsen diffusion and surface diffusion of adsorbed CO₂. To calculate the CO₂ surface flow, c_0 and q can be obtained from the adsorption isotherms of CO₂ on SiO₂. Assuming that adsorbed and gas phase CO₂ are in equilibrium at the membrane inlet, c_0 is the amount of adsorbed CO₂ corresponding to the membrane temperature and the CO₂ partial pressure of in the feed stream. Since the amount of adsorbed CO₂ at a given pressure decreases with increasing temperature, c_0 will decrease as T increases. The surface concentration at the outlet c_L is set to zero, since the CO₂ partial pressure in the sweep stream is negligible.

The heat of adsorption ΔH is an upper bound for q , the activation barrier to surface diffusion. Sladek et al. [Sladek, 1974] have shown that an expression of the form $D = D_0 \exp(\frac{-a\Delta H}{RT})$, with a between 0.1 and 0.5 correlates strongly with measurements of D over 11 orders of magnitude, for various adsorbate-surface systems. ΔH is found to be weakly dependent on concentration, and has an average value of 18.5 kJ/mol. This is consistent with the Henry's law (dilute limit) behavior indicated by the nearly linear isotherms. Surface flow of CO₂ is now given by

$$Q_{surf}^{CO_2} = -2\pi r D_0 \exp(\frac{-a\Delta H}{RT}) \frac{c_0}{L}, \quad (2-6)$$

where $D_0 = 1.6 \times 10^{-6} \text{ m}^2/\text{s}$, $a=0.45$ and ΔH is the heat of adsorption [Sladek, 1974]. The temperature dependence of $Q_{surf}^{CO_2}$ will be determined by the interplay between c_0 which decreases with temperature and D which increases with temperature.

The CO₂ selectivity of the membrane is defined as

$$S_{CO_2/He} = \frac{Q^{CO_2}}{Q^{H_2}} = \frac{Q_{Kn}^{CO_2} + Q_{surf}^{CO_2}}{Q_{Kn}^{H_2}} = 0.2 + \frac{Q_{surf}^{CO_2}}{Q_{Kn}^{H_2}}, \quad (2-7)$$

Substituting for $Q_{Kn}^{H_2}$ and $Q_{surf}^{CO_2}$ from Eq.1 and Eq.4 respectively,

$$S_{CO_2/H_2} = 0.21 + D_0 \exp(\frac{-a\Delta H}{RT}) \frac{3c_0}{r^2 \Delta P} \sqrt{\frac{\pi MRT}{8}}. \quad (2-8)$$

c_0 is calculated from the adsorption isotherms at the specific conditions of temperature and pressure. The only free parameter in the expression for selectivity in Eq.2-8 is the pore radius. For constant r , S_{CO_2/H_2} decreases with increasing temperature, due to a reduction in surface flow as the CO₂ adsorption at the pore inlet decreases. S_{CO_2/H_2} decreases with increasing r due to reduced surface-to-volume ratio.

A design curve for a reverse-selective CO₂/H₂ membrane can be used to determine the critical pore diameter to achieve a target selectivity for a material system defined by its heat of

adsorption and the concentration of CO₂ at the target operating conditions. The curve accounts for Knudsen diffusion of both gases and CO₂ surface transport but not pore blocking. For example, at 250 °C with a partial pressure differential across a membrane of 1x10⁵ Pa, Figure 2-1 shows the critical pore diameter required to achieve a selectivity of 60 for CO₂/H₂. Promising candidate materials possess combinations of c₀ and ΔH that fall *above* the constraint line. This line shifts upward with increasing pore radius, making it more difficult to achieve the desired selectivity in structures with larger pores. Physically, this is due to the higher degree of surface diffusion needed to offset the increased Knudsen flow through the larger pores. This analysis indicates that the membrane structure should possess small pores and comprise materials with high c₀ and low ΔH.

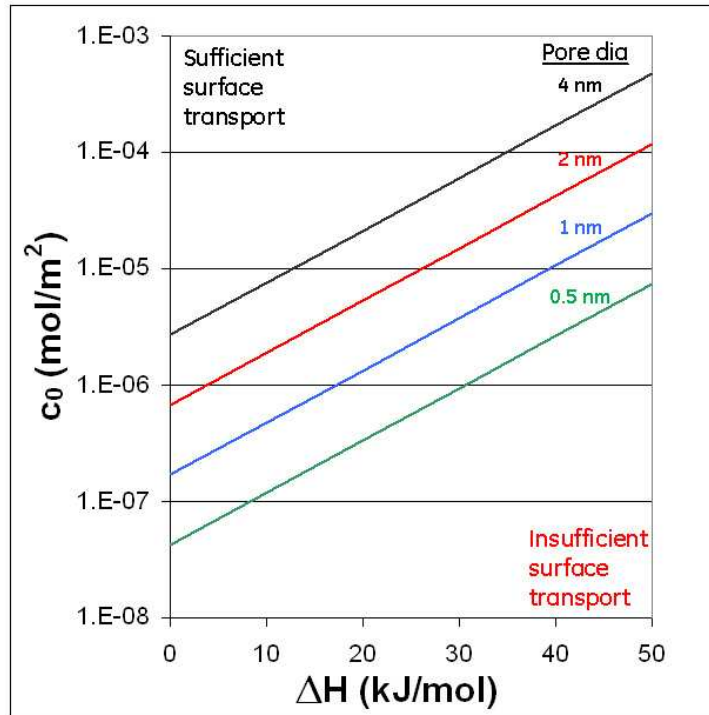


Figure 2-1. Calculated required adsorption properties for CO₂/H₂ selectivity of 60 at 250 °C as a function of the pore diameter. Materials parameters from the region below the line of constant pore diameter do not provide sufficient surface transport to meet the selectivity target and materials parameters from the region above the line do meet the selectivity target.

2.2 SYNTHESIS OF MESOPOROUS INORGANIC MEMBRANE STRUCTURES

A process for making repeatable silica membranes was developed. Since silica is known to be reverse-selective at room temperature, it can be used to verify the design model. Sol-gel processing is a versatile, solution-based method for producing particles, thin films, and monoliths with finely controlled microstructure and morphology.[Brinker, 1990][Lin,2003] These methods utilize a multi-step procedure in which a liquid sol is prepared, processed into gels of the desired morphology, and, optionally, heat-treated to densify or adjust the crystallinity of the ceramic. Control over the microstructure derives from a wide range of factors including the sol composition, its aging history, the gelation conditions, and post-gelation treatments.

Silica is a model system for sol-gel processing because of the availability of precursors – including organometallics and bio-ligands, and its well-understood chemistry [Brinker, 1990]. Of particular interest are sols comprising molecular precursors, which enable tight control of composition on the molecular scale as well as the ability to fine tune the microstructure. Depending on the processing conditions, molecular precursor-based sols react to form particulate or polymeric sols that produce particles, bulk ceramics, coatings, or membranes. Alkoxide precursors offer the possibility of polymeric and particulate microstructures. One limit is polymeric microstructures – cross-linked chains of silica oligomers. The other limit is particulate microstructures – particles that nucleate and grow.

Focusing on sol-gel derived silica films, suitable material properties are achieved only by properly aging of the sol, typically for hours to days, to produce an optimized distribution of oligomers before film deposition. Due to the wide range of compositions and required properties, optimized conditions are commonly determined on a case-by-case basis. This distribution is important in at least two ways. First, the connectivity between silica oligomers controls the microstructure of the gelled material. Second, the impact of oligomer size on solution properties such as viscosity can control the deposited thickness.

The goal of this study was to produce high-flux, reverse selective silica membranes to serve as a benchmark material for the development of high temperature CO₂-selective membranes. First, a process for making microporous silica membranes was optimized to produce high selectivity, high flux membranes. To this end, key factors for controlling membrane performance were identified and controlled. One important outcome of this effort was the need to age the precursor sol to obtain defect-free structures. At room temperature, this typically required several weeks of aging, but the age time could be reduced to a few hours by heating the sol.

2.2.1 Experimental methods

CO₂ selective silica membranes with high flux have been developed based on literature approaches [Moon, 2004]. This approach involves the deposition of a thin microporous silica film on a porous support to form an asymmetric structure. The thin film imparts selectivity while the support provides mechanical stability. A critical requirement is the absence of defects, such as pinholes or macroscopic cracks, which allow fluid flow to bypass the thin film. To preclude viscous flow, the nominal diameter of a pore (pinhole) must be less than the mean free path of the gases to be separated. Moreover, for membranes that separate through a surface diffusion

mechanism, smaller pores are better (for a given porosity) because the higher surface area allows a greater contribution from surface transport.

The morphology of the film depends on the sol composition, its processing history, the conditions used to deposit the thin film, and the thermal treatments used to densify the structure. This study addresses the following categories on CO₂ transport: the effect of aging at different temperatures, the effect of spin coating conditions, multiple coating steps, overall thickness control, the effects of porogen additions, and the effect of dopant concentrations.

In order to measure the flow characteristics of the fabricated membranes a support substrate with high flux was needed. Porous alumina substrates were developed and fabricated in house. The Al₂O₃ substrates were produced by tape casting of Taimei α -alumina powder (average particle size 0.2 μ m). Silica separation layers were deposited directly on the surface of the alumina membrane supports.

Silica sols were prepared by mixing tetraethylorthosilicate (TEOS), ethanol (EtOH), water (H₂O), hydrochloric acid (HCl), and an organic porogen, typically tetrapropylammonium bromide (TPABr). All reagents were obtained from Aldrich and used as received. First, the organic porogen was added to EtOH at 50 °C while refluxing. The solution was cooled and a HCl-H₂O mixture was added to the solution. In a separate container TEOS was added to EtOH and dissolved. The two solutions were combined near room room temperature (23°C) and mixed in a covered container. The solution exhibited a weak exothermic reaction before returning to room temperature. The solution was filtered with a 450nm filter and stored in an airtight container at -3°C to prevent premature aging of the solution. Storage at low temperature slows the kinetics of the hydrolysis and condensation reactions allowing sol lifetime to be extended by 3 months as compared to 15 days at room temperature.

The final solutions were visually clear. As the sol ages the viscosity increases and causes thickness variations in a single coat that will approach 1 μ m as the solution ages. Single coatings exceeding 750 nm tended to crack during the dry and firing cycles. For accelerated aging experiments, the sol was heated to 55 °C and 75 °C using a conventional oven. After aging the sol was cooled to room temperature, the particle size was measured using dynamic light scattering, the solution was diluted, and a membrane was fabricated utilizing the spin coat technique.

Sols were characterized using visual inspection and dynamic light scattering (DLS). DLS was performed using a Brookhaven Instruments DLS system equipped with a He-Ne laser. Samples were sealed in 12 mm test tubes and inserted into a goniometer. The refractive index and solvent parameters were set based on the materials being tested. For the silica particles a refractive index of 1.45 was used. The DLS was used to determine an average sol particle size.

Spin coating was used in lieu of dip coating because the technique is well suited to reproducible fabrication of films with thicknesses less than 1 μ m. A spin coater (Model P6700, Specialty Coating Systems, Inc.) was used to deposit the sol onto porous substrates. Prior to coating, the sample was exposed to a stream of compressed air (to remove dust particles). Approximately 60

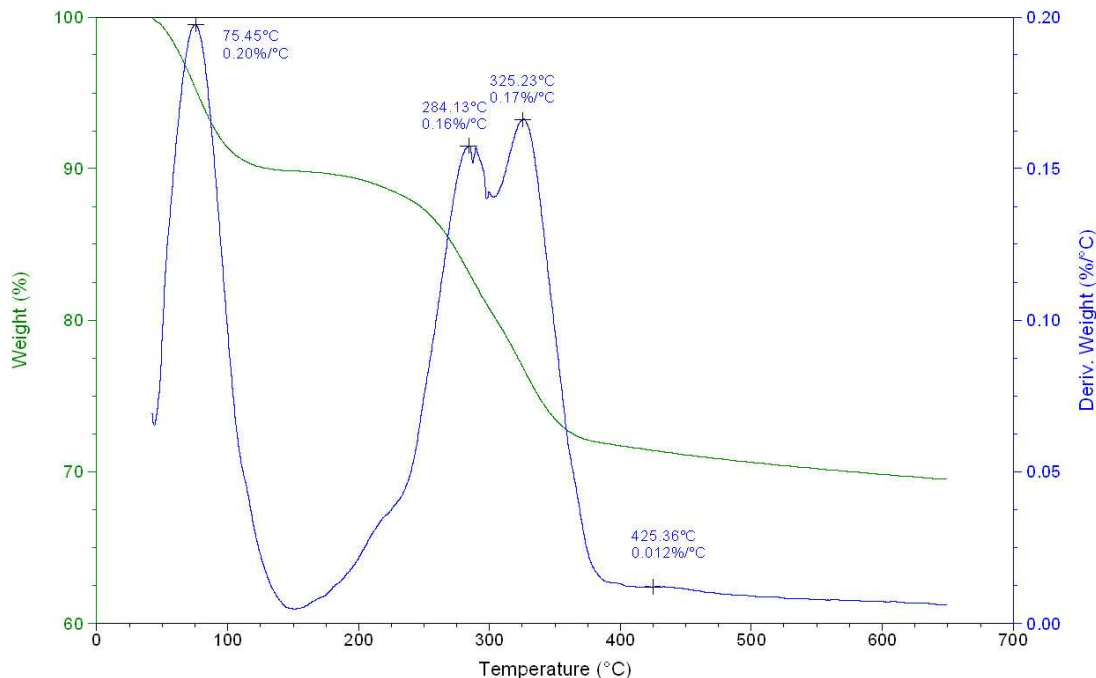


Figure 2-2. Percentage weight (green curve) and derivative weight (blue curve) as a function of temperature for silica sol as measured by thermal gravimetric analysis.

μL of sol was placed on the substrate, followed by a delay of about 5 s to allow the sol to infiltrate the substrate. The spin coating process was performed with an acceleration time of 2 seconds, dwell speed of 4000 rpm, hold time of 30 seconds, and a deceleration time of 10 seconds.

In film fabrication by sol-gel it is especially important to understand the thermal evolution of a film in order to avoiding crack formation during gas evolution and densification. To evaluate the thermal evolution of the sol-gels thermal gravimetric analysis was performed and can be seen in Figure 2-2. The derivative analysis indicated significant mass loss events at 75 °C, 284 °C and 325°C, corresponding to the loss of EtOH (boiling point 79 °C) and TPABr, respectively.

From this analysis it was determined that the sample should be heat-treated at temperatures greater than 400°C. Samples were heat-treated in air at temperatures from 500-600°C to remove the organic materials and densify the structure. Membranes were fired at a 2°C/min-heating rate to 550 °C with a two-hour hold time and furnace cool. The hold temperature of 550 °C was selected because the mass loss was complete at that temperature. A relatively slow rate (2 °C/min) was used to allow sufficient oxygen diffusion into the structure for porogen burnout and to prevent cracking of the structure due to escape of the evolved gases. Supported films fired for 2 h appeared opalescent. Powders fired for 2 h had a brownish tint due to residual carbon. Longer hold times at temperature eliminated this problem.

X-ray diffraction (XRD) was performed on powder obtained from a gelled solution to confirm the amorphous state of the silica. High angle (10-90° 2 θ) diffraction patterns were collected using a Bruker D8 Advance diffractometer equipped with a linear position-sensitive detector

(PSD-50m) manufactured by M. Braun. Nickel-filtered copper Ka radiation was used with an aperture slit of 0.6mm.

2.2.2 Defect rate measurement

Knudsen diffusion occurs in the limit where the pore dimensions are smaller than the mean free path of a gas, while viscous flow occurs when the pore dimensions are larger than the mean free path. For air at standard temperature and pressure, the mean free path is about 60 nm. Since the target pore sizes for the membranes of interest are less than 10 nm, the transport of non-adsorbing nitrogen and oxygen through a defect-free membrane is expected to occur by Knudsen diffusion. However, a synthesis method may produce occasional voids or microcracks that are large enough to permit viscous flow.

The total flow through a membrane is simply the sum of the flow through its pores. For non-adsorbing gases, the flow through “small” pores occurs by Knudsen diffusion and the flow through “large” pores occurs by viscous flow. For an adsorbing gas, an additional flow due to surface transport occurs along the pore walls. Small pores are desirable in a CO₂/H₂ selective membrane because the surface flow of CO₂ in a must be sufficiently large to impart a favorable selectivity.

For the purposes of membrane development in this program, a defect is defined as a pore that is sufficiently large to allow viscous flow. It is important to note that this is a necessary, but not sufficient condition for achieving the target selectivities. Since the selectivity in a defect-free depends on the relative amounts of surface to Knudsen flow, it is possible for a membrane to be defect-free, yet still contain pores that are too large to permit sufficient surface flow to achieve the target selectivity.

Calculation of defect rate. The defect rate is computed from the fraction of total flow that occurs due to viscous flow. For gas permeability measurements, the flows can be expressed as permeances, which normalize the flow by the membrane area and applied pressure differential. For a monodisperse population of cylindrical pores, the Knudsen and viscous permeances vary as:

$$K_{\text{Knudsen}} = \frac{\varepsilon d_p \bar{v}}{3 \tau t RT} \quad K_{\text{viscous}} = \frac{\varepsilon d_p^2 p}{32 \tau \mu t RT} \quad (2-9a, b)$$

where d_p is the pore diameter, t is the membrane thickness (cylinder length), T is the temperature, p is the gas pressure (taken here to be the average gas pressure across the membrane thickness), μ is the viscosity, ε and τ are the porosity and tortuosity, respectively, and $\bar{v} = \sqrt{8kT/\pi M}$ is the average velocity of the gas molecules. The permeability can be computed from the permeance by multiplying for the membrane thickness.

Since K_{Knudsen} is independent of pressure, while K_{viscous} increases linearly with pressure, the Knudsen and viscous components of flow through the membrane can be quantified by measuring membrane permeance for a range of differential pressures. Since Equations 2-9a and 2-9b exhibit

different functional dependences on pressure, the relative contributions from Knudsen and viscous flow can be determined by plotting the permeance vs. the average pressure. The permeance due to Knudsen flow is independent of pressure while the viscous flow increases linearly with pressure. The intercept gives the Knudsen contribution with viscous flow accounting for the balance. The defect rate was computed by dividing the viscous permeance by the total permeance measured at $\Delta P = 3.4 \times 10^4$ Pa (5 psi). The defect rate, f , is defined as $K_{viscous} / K_{eff}$ at the average measurement pressure. This analysis is consistent to similar analyses using the dusty gas model described in the open literature.

2.2.3 Process development for silica membranes

The thickness requirement for producing membranes free of viscous defects was determined by measuring the defect rate as a function of thickness. Two main populations of defects were observed, as shown in Figure 2-3 and Figure 2-4. *Non-filling defects* occurred when the sol infiltrated into the substrate to leave behind large pores. These defects occurred because of insufficient mass in the layer to completely fill the pores of the underlying substrate. In previous work, non-filling defects have been mitigated through the use of intermediate layers with progressively smaller pore sizes. *Cracking defects* were caused by residual stresses in thick silica films. The critical thickness is determined by the shrinkage rate and mechanical properties of the film. Typical critical thicknesses that have been reported in the literature for comparable sol compositions are about 1 μm .

Gas permeability measurements were used to quantify the rate of defects as a function of film thickness. The defect rate was computed as the fraction of flow through the membrane attributable to viscous flow. This corresponds to pores with a diameter larger than about 60 nm (the mean free path of the test gas, air) and can be inferred from the pressure dependence of the flow. Figure 2-3 shows the relationship between the defect rate and thickness.

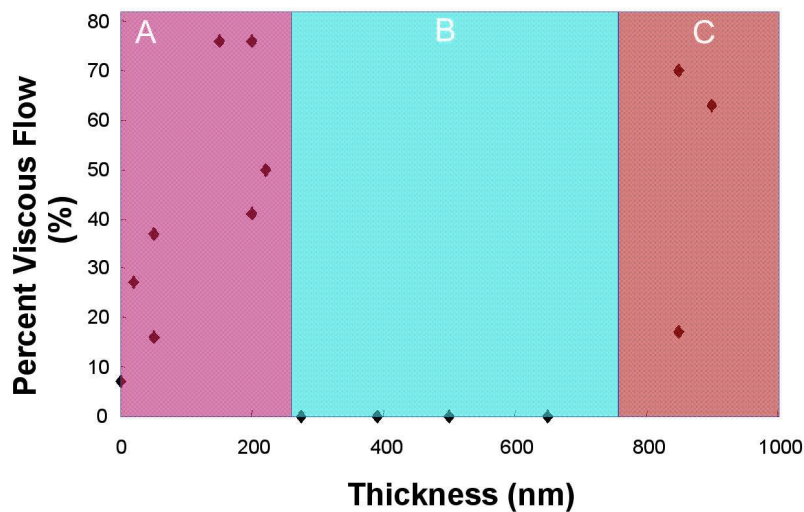


Figure 2-3. Viscous flow through the membrane as a function of thickness. Three regions were identified a) defects from incomplete filling, b) viscous defect-free, and c) defects from cracking.

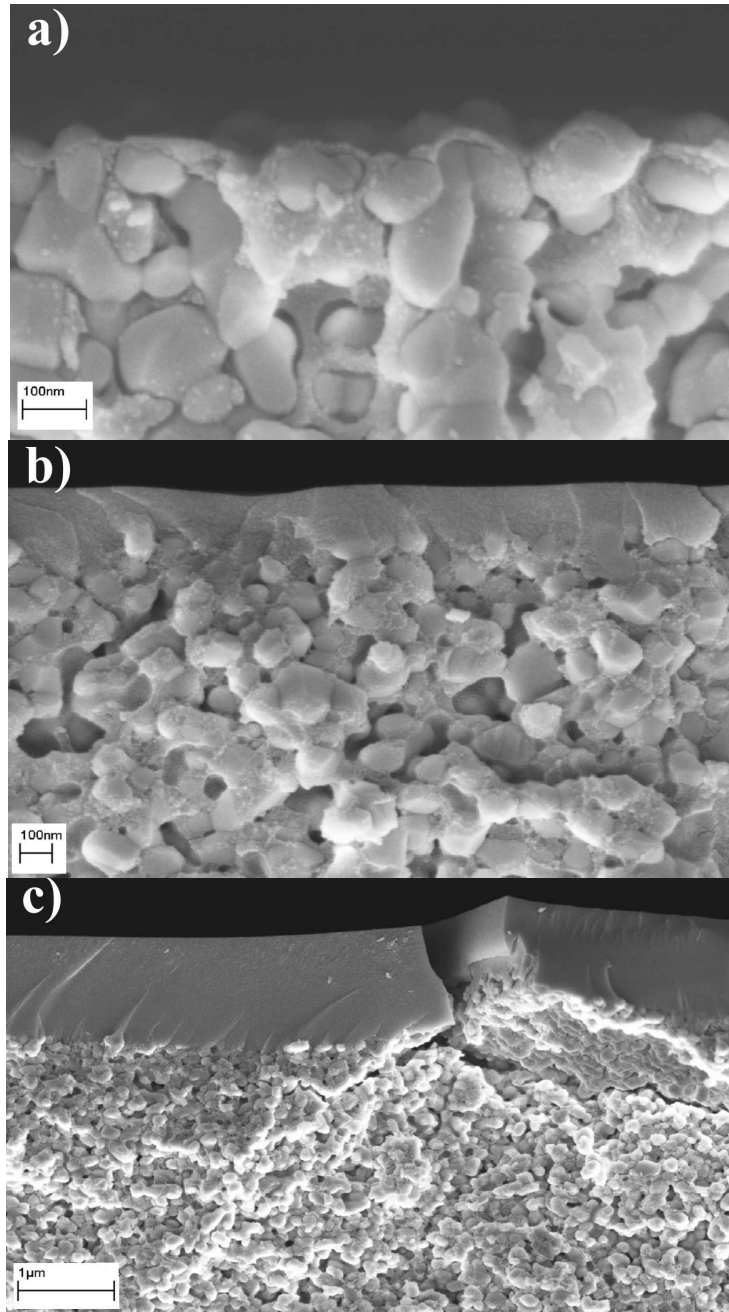


Figure 2-4. Scanning electron micrographs of silica membranes for the three regions identified in Figure 2-3 a) incompletely filled membrane, b) viscous defect-free membrane and c) cracking defect.

Below about 250 nm and above about 750 nm in thickness, the membrane shows substantial viscous flow. For thinner films, SEM characterization of the microstructure revealed non-filling defects, due to infiltration of the sol into the porous support during the spin-coating process. Conversely, the thicker films developed crack defects, resulting from excessive stress during the processing cycle. These values provide upper and lower targets for the film thickness. After

further work it was found that to obtain high flux and minimize crack formation a target thickness near the lower limit became the objective.

It is noteworthy that, in both extremes that the contribution to viscous flow exceeds that of the uncoated porous support (7%). This can be explained by the reduction in flow through pores smaller than the Knudsen limit. While the overall flow is lower, the relative contribution from viscous flow is enhanced. This is a magnification of the viscous flow contribution as Knudsen pores are filled. That demonstrates the importance for processing completely viscous defect-free films.

Films of the desired thickness can be fabricated through either a single coating step or through multiple coatings. A single coating approach offers advantages in simplicity and cycle time. The infiltration of the solution controls the first coat thickness. Virtually no overlayer was formed using sols aged a single day, while a thick overlayer (with thickness comparable to a film spun on a silicon wafer) was obtained after 25 days of aging.

Depositing multiple thin layers on top of each other can form films of a comparable thickness. The advantage of such an approach is the possibility of sealing any defects that form during previous coats. In a multi-step coating process, the thickness of the first layer can be adjusted to sufficiently seal the pores of the support through the aging time. The minimum thickness for this “overcoat” was 10 nm. For the porous support used in this work, a properly aged first layer eliminates the need for an “intermediate” layer between the support and the silica film.

Figure 2-5 shows the relationship between sol age and the total membrane thickness (as measured by SEM). First coats prepared using sols aged less than a week did not show any evidence of an overcoat. Multiple coats, however, were effective in eventually producing a defect-free film of the desired thickness. For sols aged up to a week, six coats were typically required. After 10 days of aging, membranes could be prepared with as few as two coats. Figure 2-5 also shows the relative thicknesses of a first and second coat for sols aged up to 25 days. The large difference between first and second coats is due to solution infiltration into the substrate. At room temperature, sols must be aged at least 7 days to produce a defect-free membrane using 2 to 3 coating steps.

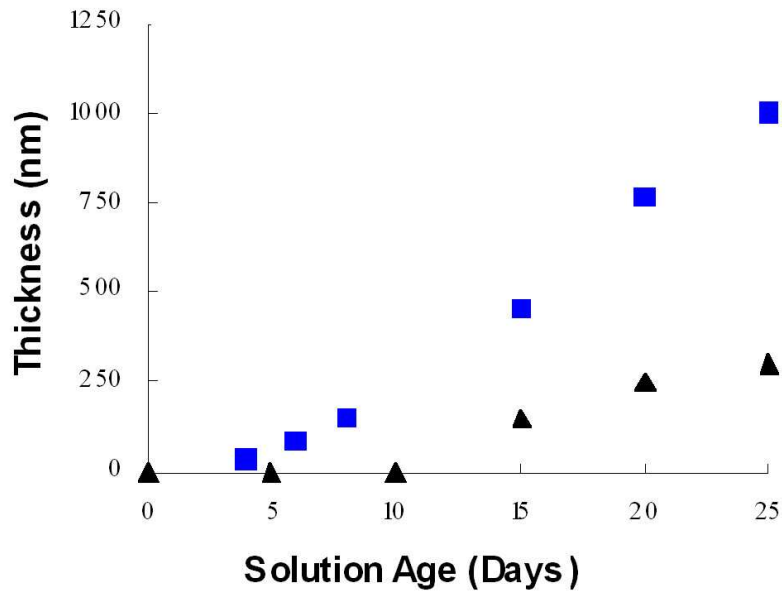


Figure 2-5. Thickness of the silica layer as a function of solution aging time for the first coating layer (black triangles) and second coating layer (blue squares).

A number of processing parameters affect the thickness of a spun layer. These can be grouped into two categories: sol properties and coating process parameters. Sol properties include variables such as sol composition and aging history. These factors control the rate of oligomer growth in the silica sol, which is responsible for the formation of a continuous polymeric structure. Coating process parameters include factors such as spin speed, dilution, and calcination conditions. The spin coating conditions control the thickness of the cast film, which undergoes additional structural evolution during heating to form the final film. Although their effects will be described separately, these factors are coupled in the sense that the microstructure is dependent on the factors in a non-linear fashion.

Age time is a critical factor in obtaining a sol that produces a film with the desired thickness. Physically, the age time determines the extent of oligomerization in the sol before it is spun into a film. Longer age times correspond to larger oligomers, which impact the viscosity, the extent of infiltration into the pores of the substrate, and the density of the as-cast film. The effect of age time is directly related to the rate of condensation of silica monomers with silica oligomers. This, in turn, is sensitive to the temperature at which the sol is aged. This can be seen in Figure 2-6, which plots the thickness of the first layer for sols aged at room temperature and 55 °C.

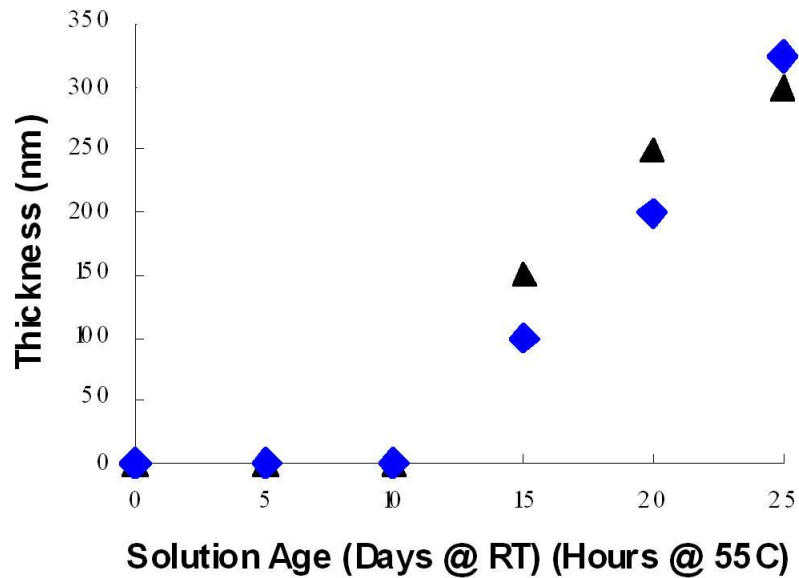


Figure 2-6. Membrane thickness as a function of solution age for sol aged at room temperature (black triangles) and aged at 55 °C (blue diamonds).

DLS was used as a gage to monitor the state of the oligomer formation and particle growth in the solution. This provided a means of comparing the extent of oligomerization for different age time-temperature histories. Figure 2-7 plots oligomer size versus age time for samples aged at room temperature and 55 °C and 75 °C. The oligomer size increases monotonically with time, in a manner suggestive of the thickness trend. Figure 2-8 plots the thickness of a single coat membrane against the oligomer size in the sol used in to fabricate the membrane.

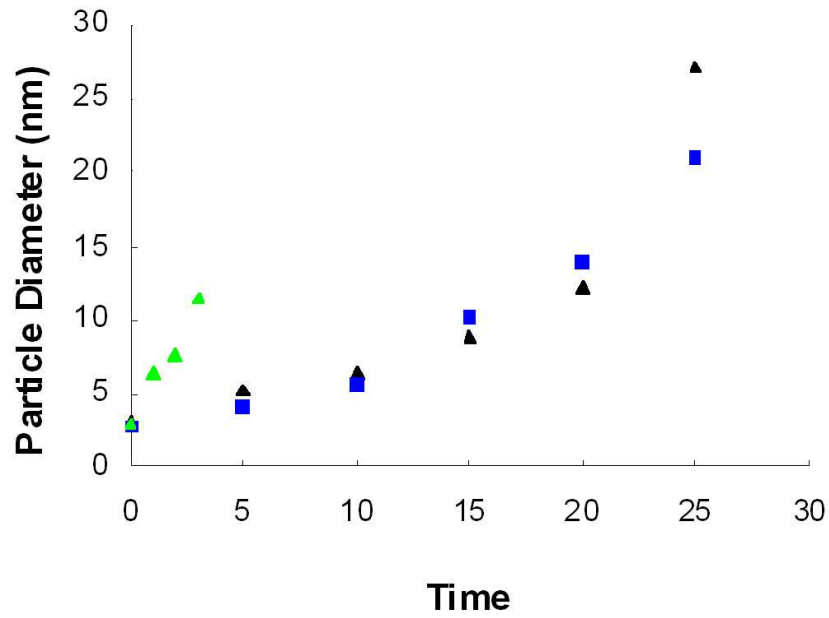


Figure 2-7. Particle diameter as a function of time for sols aged at room temperature (blue squares with time measured in days), sols aged at 55 °C (black triangles with time measured in hours) and sols aged at 75 °C (green triangles with time measured in hours).

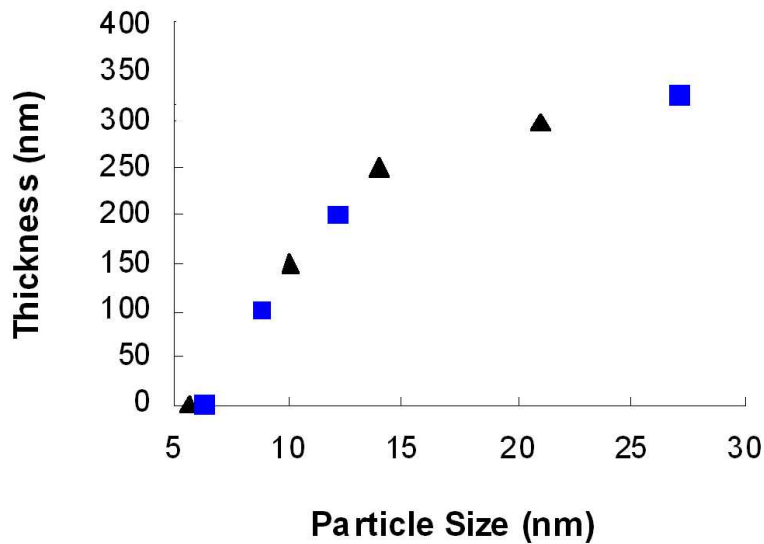


Figure 2-8. Membrane thickness as a function of sol particle size for room temperature aged sol (black triangles) and sol aged at 55 °C (blue squares).

Once normalized on the basis of oligomer size, the thickness of membrane produced from sols aged at room temperature and 55 °C collapse onto a single curve. No appreciable overlayer was formed for sols with oligomers less than about 7 nm in size, independent of the aging conditions. However, above this size, the thickness increased monotonically. DLS oligomer size was determined to be a proxy for age time in predicting the thickness of spun membranes

2.2.4 Room temperature separation measurements

Gas separation measurements were performed in a tube-in-tube type rig, shown schematically in Figure 2-9. Disc-shaped membranes were sealed with epoxy onto the ends of the inner tubes. The feed stream (50-50 mixture of He-CO₂ or H₂-CO₂) flowed through the outer tube, past the membrane, at a rate of about 1 L/min. The permeate was collected from the inner tube by an nitrogen sweep stream flowing at 3 L/min. The transmembrane pressure differential was varied from 3.4x10⁴ Pa (5 psi) to 1.38x10⁵ (20 psi), with the low pressure side at 1.01x10⁵ Pa (1 atm). The sweep stream was sampled continuously by a capillary tube and analyzed by a quadrupole mass spectrometer (Hiden Analytical HPR20) using the secondary electron multiplier detection mode.

Reverse selectivity of viscous defect-free silica membranes was measured at room temperature with a gas mixture of CO₂/He. Enhanced surface flows of CO₂ relative to He were observed as shown in the histogram in Figure 2-10. Selectivities as high as 12 were measured. These data demonstrated the efficacy of the process for defect-free silica films.

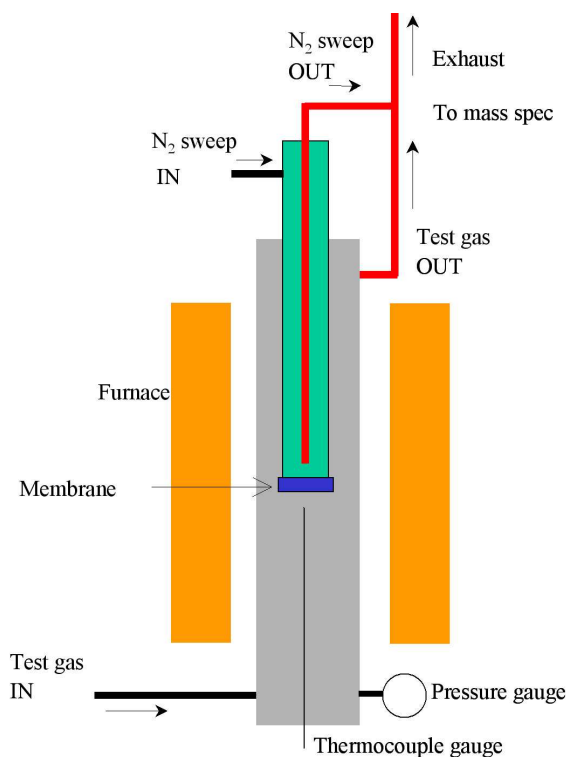


Figure 2-9. Schematic of test rig for measurement of room temperature gas separation

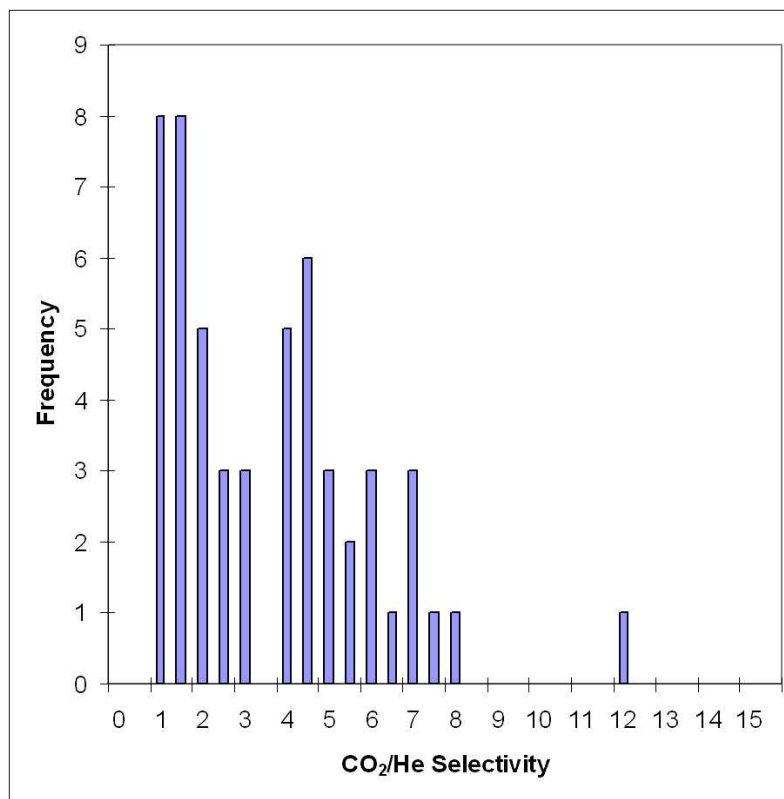


Figure 2-10. Histogram of room temperature CO₂/He separation observed for viscous defect-free silica membranes

Different porogens were incorporated into the silica in order to study the effect of changing the size and chain length of the porogen. It has been proposed in literature that the porogen size and chain length controls the pore size and distribution. This has been attributed to the incorporation of the porogen into the microstructure. A list of the porogens used in this study are shown in Table 2-1. The porogens were selected based on differentiation in chain length and branching. All of the porogens were added to the ethanol solution at 50°C and refluxed for at least ten minutes before proceeding with the process outlined in the previous section.

Measurements of CO₂/H₂ separation through membranes using a variety of porogen types is shown in Table 2-2. While CO₂/H₂ selectivity as high as 10 was observed using the TPABr porogen, typical separation factors and range is given in the Table 2-2. There was no significant effect of porogen type on separation behavior. This is most likely due to the fact that the porogen alters the oligimer formation during solution aging. The difference between our study and literature results is that oligimer evolution is monitored and all of the solutions were aged until ~10nm particles were achieved before coating the substrates.

Table 2-1. Porogens evaluated for effect on pore structure in silica membranes

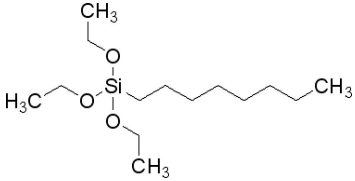
Porogen name	Chemical structure	Formula	Molecular weight
Tetrapropylammonium Bromide (TPABr)	$\begin{array}{c} \text{CH}_2\text{CH}_2\text{CH}_3 \\ \\ \text{CH}_3\text{CH}_2\text{CH}_2-\text{N}^+-\text{CH}_2\text{CH}_2\text{CH}_3 \\ \\ \text{CH}_2\text{CH}_2\text{CH}_3 \end{array} \quad \text{Br}^-$	$(\text{CH}_3\text{CH}_2\text{CH}_2)_4\text{N}(\text{Br})$	266.3
Tetramethylammonium Bromide (TMABr)	$\begin{array}{c} \text{CH}_3 \\ \\ \text{CH}_3-\text{N}^+-\text{CH}_3 \\ \\ \text{CH}_3 \end{array} \quad \text{Br}^-$	$(\text{CH}_3)_4\text{N}(\text{Br})$	154.1
Didecyldimethylammonium Bromide (DDABr)	$\begin{array}{c} \text{CH}_3 \\ \\ \text{CH}_3(\text{CH}_2)_8\text{CH}_2-\text{N}^+-\text{CH}_2(\text{CH}_2)_8\text{CH}_3 \\ \\ \text{CH}_3 \end{array} \quad \text{Br}^-$	$[\text{CH}_3(\text{CH}_2)_9]_2\text{N}(\text{CH}_3)_2\text{Br}$	406.5
Brij 56	$\text{C}_{16}\text{H}_{33}(\text{OCH}_2\text{CH}_2)_n\text{OH}$ <p style="text-align: center;">$n \sim 10$</p>	$\text{C}_{16}\text{H}_{22}(\text{OCH}_2\text{CH}_2)_n\text{OH}$, $n \sim 10$	Avg 683
Octyltriethoxysilane (OTES)		$\text{CH}_3(\text{CH}_2)_7\text{Si}(\text{OC}_2\text{H}_5)_3$	276.5
Methyltriethoxysilane (MTES)	$\begin{array}{c} \text{OCH}_2\text{CH}_3 \\ \\ \text{CH}_3-\text{Si}-\text{OCH}_2\text{CH}_3 \\ \\ \text{OCH}_2\text{CH}_3 \end{array}$	$\text{CH}_3\text{Si}(\text{OC}_2\text{H}_5)_3$	178.3

Table 2-2. Porogen type, CO₂ permeance, H₂ permeance and CO₂/H₂ selectivity at room temperature

	CO ₂ Permeance (mol/m ² s Pa)	H ₂ Permeance (mol/m ² s Pa)	CO ₂ /H ₂ Selectivity
TPABr	2.5×10^{-7}	7.3×10^{-8}	2.4 ± 0.7
TMABr	1.1×10^{-7}	4.8×10^{-8}	2.3
DDABr	1.2×10^{-6}	6.2×10^{-7}	2.0
Brij 56	4.9×10^{-7}	2.5×10^{-7}	2.0
OTES	1.1×10^{-6}	5.3×10^{-7}	2.2
MTES	4.1×10^{-8}	4.9×10^{-8}	0.8

A transmission electron microscopy image of a silica membrane with TPABr porogen is shown in Figure 2-11. It appears that the porogen segregated within each of the coating layers. The film in the TEM micrograph below was applied using the standard procedure for making reverse selective samples from a TPABr-Silica sol. The interfaces between the consecutive films are traced to show how the porogen is segregating during coating. A more homogeneous distribution of the porogen throughout the membrane structure may be required for optimized gas separation characteristics.

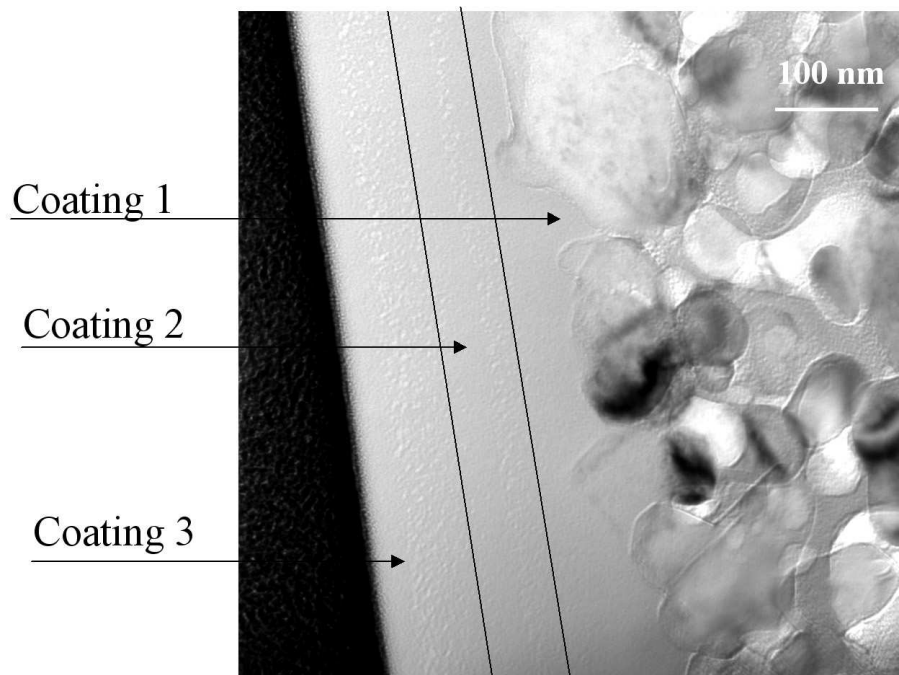


Figure 2-11. Transmission electron microscopy image of a reverse-selective silica film produced with three sequential coating applications. The porogen had segregated within the layers.

2.3 MODEL FOR HIGH TEMPERATURE MEMBRANE PERFORMANCE

As described in section 2.1, the expression for CO₂/H₂ selectivity through a membrane with CO₂ surface diffusion is given by

$$S_{CO_2/H_2} = 0.21 + D_0 \exp\left(\frac{-a\Delta H}{RT}\right) \frac{3c_0}{r^2\Delta P} \sqrt{\frac{\pi MRT}{8}} \quad (2-10)$$

where the constants are given by $D_0 = 1.6 \times 10^{-6} \text{ m}^2/\text{s}$, $a=0.45$, R is the universal gas constant, T is temperature, and M is the molecular weight of H₂. The properties of the material are given by ΔH , which is the heat of adsorption of CO₂ and $c_0/\Delta P$, which is the surface concentration of CO₂ for a change in pressure. Those quantities can be obtained from adsorption isotherms. One microstructural parameter, r , which is the effective pore radius, will be taken as a fitting parameter.

The silica membranes described in Section 2.2 were used to validate the model for high temperature membrane performance. The adsorption properties of silica were measured using a chemisorption measurement on silica powder. The selectivity for CO₂/H₂ was measured as a function of temperature and compared with single gas permeation measurements to infer the average pore radius. Evidence for pore blocking was obtained and a quantitative estimate of its effect was produced.

2.3.1 Adsorption measurements

Both ΔH and $c_0/\Delta P$ can be calculated from adsorption isotherms for CO₂ adsorption on candidate metal oxide powders. An apparatus for measuring adsorption isotherms (Micromeritics ASAP 2020 Chemi) was used. Isotherms were obtained by measuring the CO₂ uptake of a high surface area sample of known mass, as a function of pressure. The sample was dosed with a known amount of CO₂ (determined by the set point pressure) and the decrease in pressure due to CO₂ adsorption was monitored. Once the pressure was stable, the process was repeated, until the sample surface was saturated and the set point pressure was maintained without a pressure drop. The process was repeated at the next set point pressure. The amount of CO₂ adsorbed on the sample surface at every pressure can be accurately determined by this method. The sample temperature was kept constant during these measurements. $c_0/\Delta P$ was obtained directly from the adsorption isotherms. The isotheric heat of adsorption, ΔH , was calculated from a series of isotherms as described below. Specific surface areas of the samples were measured by N₂ adsorption.

CO₂ adsorption measurements were made SiO₂ powders with a surface area of 800 m²/g. Isotherms were obtained at temperatures ranging from 100 °C to 500 °C. The sample surfaces were regenerated, between isotherms, by annealing at 600 °C in a He atmosphere to remove remnant adsorbates. These results were benchmarked against adsorption isotherm measurements and analyses have been reported in the literature for SiO₂ [deLange, 1995].

CO₂ adsorption isotherms for SiO₂ are plotted in Figure 2-12. The plot shows that CO₂ adsorption decreased with increasing temperature. At a given temperature and pressure, $c_0/\Delta P$ can be obtained from these curves. The isotheric heat of adsorption was determined from the

slopes of the isotherms by the Van't Hoff equation, $\Delta H = -R \frac{d \ln P}{d(1/T)}$. The heat of adsorption as a

function of surface coverage is plotted in Figure 2-13. ΔH is found to be weakly dependent on concentration, and has an average value of 18.5 kJ/mol. This is consistent with the Henry's law (dilute limit) behavior indicated by the nearly linear isotherms. In Figure 2-14, $c_0/\Delta P$ calculated from the adsorption isotherms is plotted as a function of temperature. Since the CO_2 isotherms for SiO_2 are nearly linear, this quantity is equivalent to the isotherm slope.

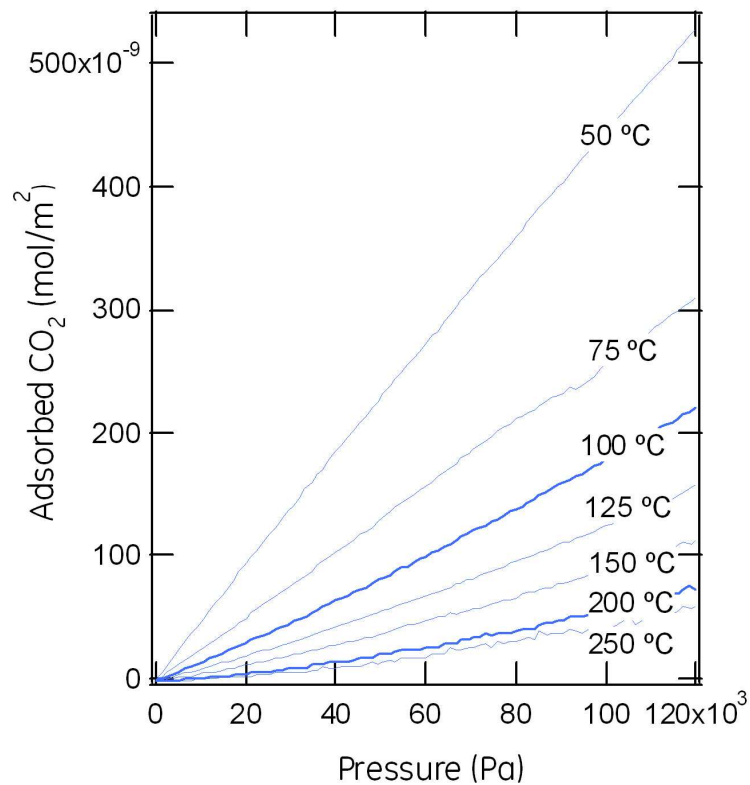


Figure 2-12. CO_2 adsorption isotherms for SiO_2 as a function of pressure.

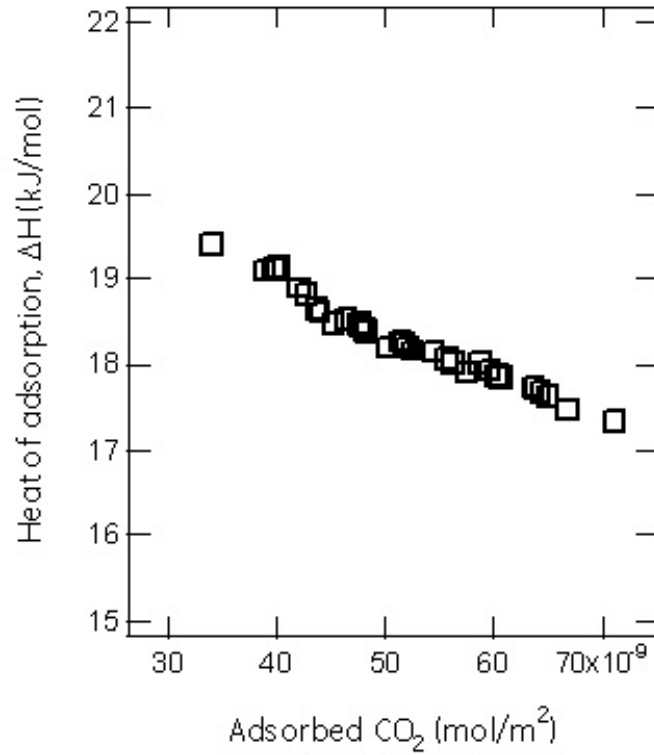


Figure 2-13. Isothermic heat of adsorption for SiO₂ as a function of adsorbed CO₂ concentration.

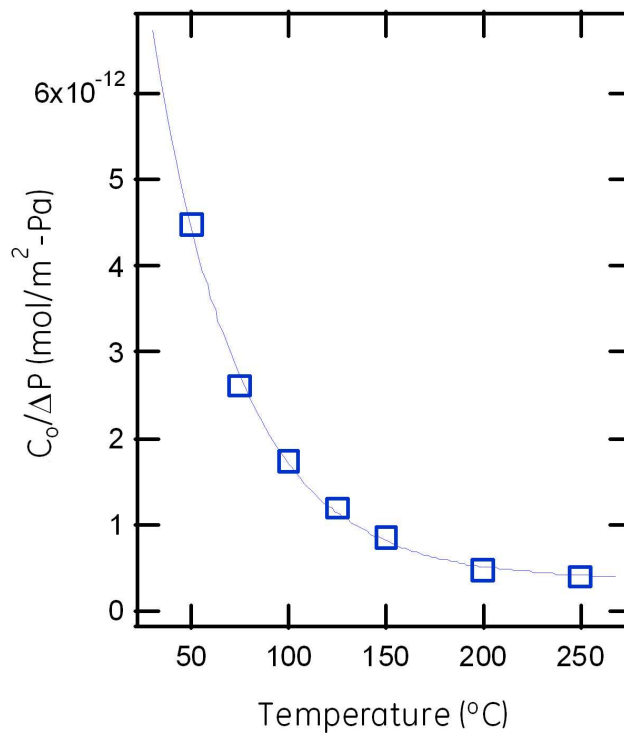


Figure 2-14. $c_0/\Delta P$ at 82 Pa, calculated from the CO₂ adsorption isotherms

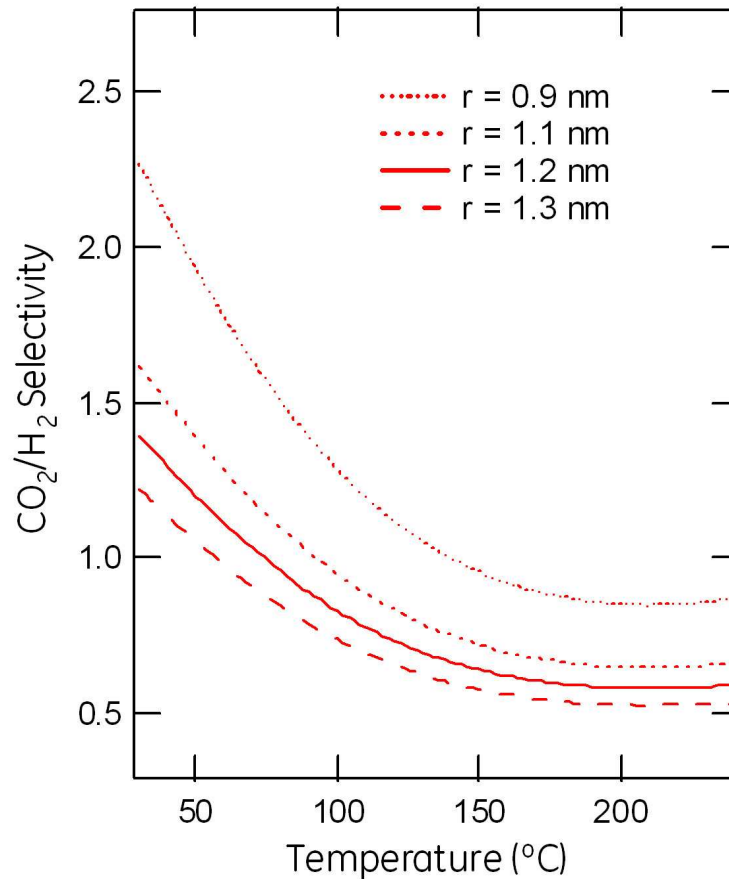


Figure 2-15. CO₂/H₂ selectivity predictions as function of temperature, for pore radii ranging from 0.9 nm to 1.3 nm.

A set of predicted curves for the CO₂/H₂ selectivity of a membrane as a function of temperature is given in Figure 2-15 for a range of pore sizes. These predictions will be compared with measured membrane data in the next section. The decrease in selectivity with temperature is due to the reduction in the adsorbed concentration of CO₂ with temperature as shown in Figure 2-14.

2.3.2 Membrane measurements

A test rig for performing gas separation measurements as a function of temperature is shown schematically in Figure 2-16. The rig consisted of a high pressure up-stream volume and an atmospheric pressure down-stream volume, partitioned by the disc-shaped membrane, sandwiched between gas-tight silicone seals. The feed stream, typically equimolar H₂-CO₂ or He-CO₂ mixtures, flowed through the up-stream volume and past the membrane, at a rate of 0.25 L/min. Membrane permeate was collected by an N₂ sweep stream flowing through the down-stream volume at 1.5 L/min. The total trans-membrane pressure differential, ΔP , was varied from 3.4×10^4 Pa (5 psi) to 1.72×10^5 (25 psi). The sweep stream was sampled continuously via a capillary tube and analyzed by a quadrupole mass spectrometer (Hiden Analytical HPR20) using a secondary electron multiplier detector.

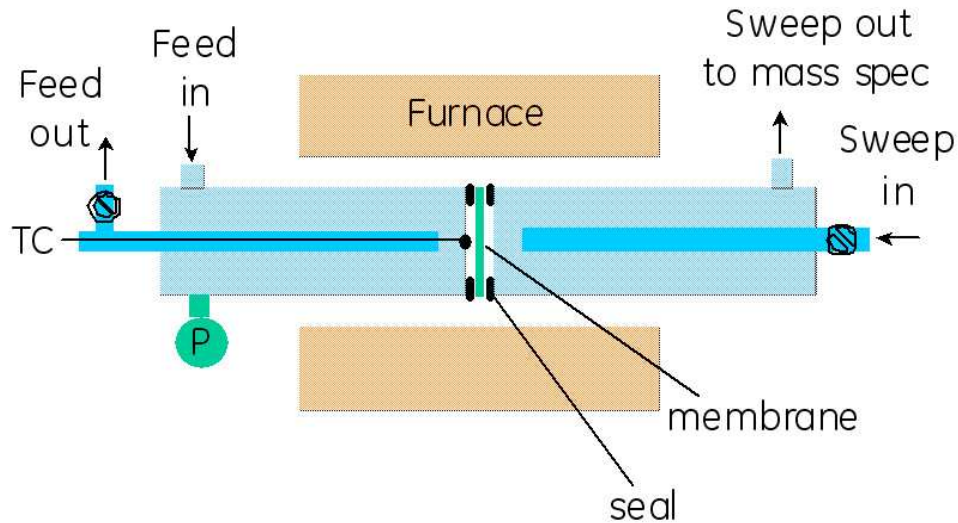


Figure 2-16. Membrane separation test rig

For high temperature gas separation measurements, the test rig was heated by a furnace to a maximum temperature of 250 °C. Sample temperature was monitored by a thermocouple located near the membrane. Gas separation and temperature data were continuously recorded during heat-up and cool-down of the rig. The heating measurements were performed at a fixed ΔP of 10 psi, which corresponds to a CO_2 or H_2 partial pressure of 8.2×10^4 Pa (12 psi).

The results of the high temperature H_2 - CO_2 separation and He - CO_2 separation by a SiO_2 membrane are shown in Figure 2-17 for permeances and Figure 2-18 for CO_2/H_2 selectivities as a function of temperature. The room temperature CO_2 and H_2 permeances of the membrane are about 5×10^{-7} mol/m²-s-Pa and 2×10^{-7} mol/m²-s-Pa, respectively, and the corresponding CO_2/H_2 selectivity is about 2.5. As the membrane temperature increases, the CO_2 permeance reduces continuously, while the H_2 permeance increases and then reaches a plateau at a temperature of about 140 °C. The CO_2/H_2 selectivity decreases towards the CO_2/H_2 Knudsen selectivity of 0.2 as the temperature increases. The plots in Figure 2-17 represent measurements made during consecutive cooling, heating and cooling runs. The run-to-run agreement is extremely good, showing that the microstructure and transport behavior of the membrane are not significantly affected by thermal cycling.

The CO_2 permeances from the CO_2 -He and CO_2 - H_2 experiments shown in Figure 2-17 are indistinguishable, implying that for these two gas pairs, the CO_2 transport through the membrane pores takes place independent of the other gas species. The temperature evolution of the He permeance is qualitatively similar to that of the H_2 permeance, but the magnitude of the He permeance is lower. The resulting CO_2/He selectivity is nearly 4 at room temperature and decreases with increasing temperature, approaching 0.3, the CO_2/He Knudsen selectivity. Assuming both He and H_2 transport take place by Knudsen diffusion, a CO_2/H_2 selectivity curve can be calculated from the CO_2/He selectivity data, by applying a Knudsen correction to the He permeance. The H_2/He Knudsen ratio is $\sqrt{2}$, and the calculated CO_2/H_2 selectivity is given by

the relationship, $S_{CO_2/H_2} = \frac{S_{CO_2/He}}{\sqrt{2}}$. This curve, also plotted in Figure 2-18, shows good agreement with the measured CO₂/H₂ selectivity over the entire temperature range and provides evidence for predominantly Knudsen diffusion of H₂ and He.

Since Knudsen permeance decreases with temperature, an increase in H₂ and He permeance with temperature is unexpected. A possible explanation is that the effective pore radius for Knudsen diffusion is smaller at low temperatures, due to adsorbed CO₂ molecules. As the temperatures rises, the amount of adsorbed CO₂ decreases, and the effective pore radius increases, and eventually becoming equal to the actual radius.

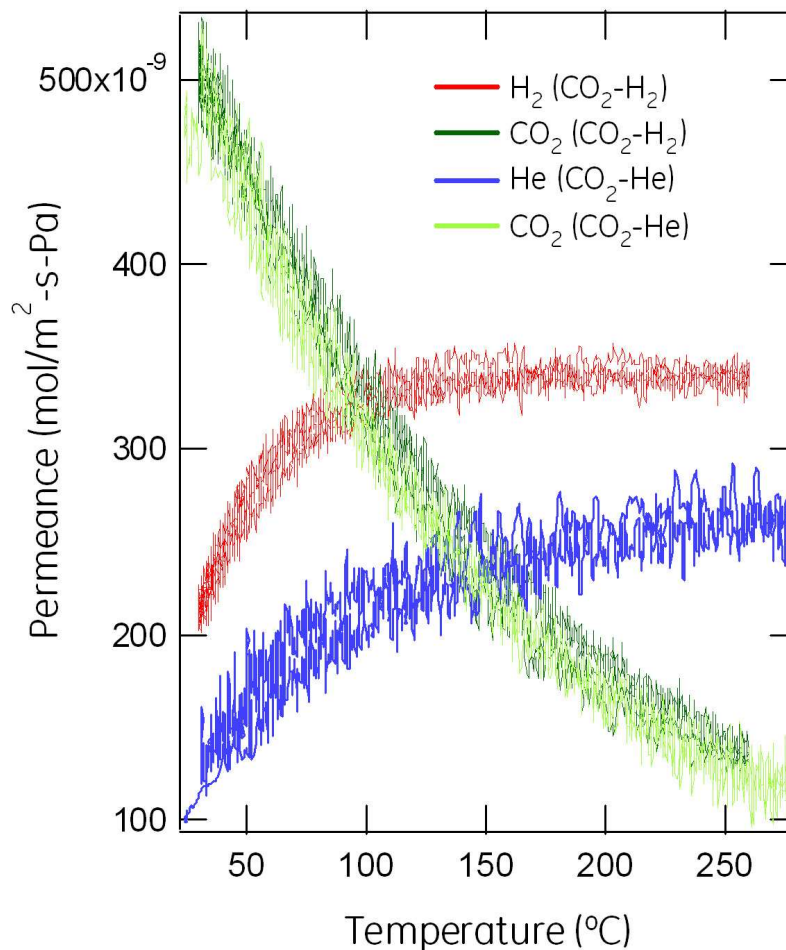


Figure 2-17. CO₂-H₂ (CO₂ permeance in dark green and H₂ permeance in red) and CO₂-He (CO₂ permeance in light green and He permeance in blue) separation performance of SiO₂ membrane.

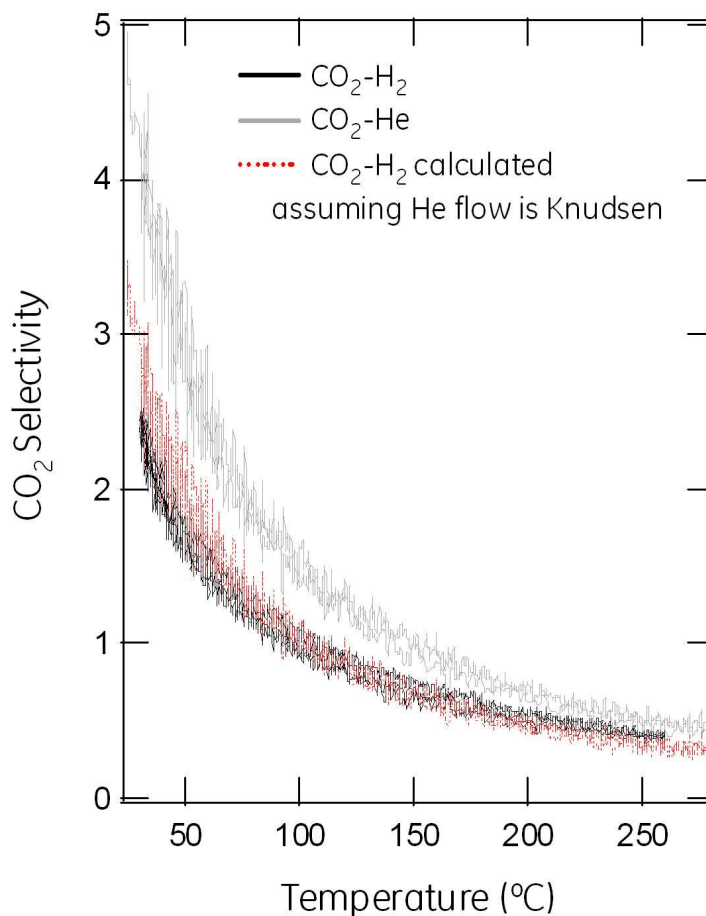


Figure 2-18. CO₂ selectivity as function of temperature for CO₂-H₂ (black curve), CO₂-He (gray curve) and CO₂-H₂ predicted from scaling CO₂-He data by Knudsen diffusion differences (red curve)

This hypothesis can be tested by comparing the permeance of pure He to the permeance of He from a He-CO₂ feed, through the same membrane. If the increase in He permeance with rising temperature is due to CO₂ pore-blocking, then this rise would be absent in the pure He measurement. Pure He and pure CO₂ permeance were measured in a similar manner to the mixed gas measurements. These measurements were followed by a He-CO₂ measurement. The ΔP for the pure gas measurements was adjusted such that partial pressure would be the same as that of each gas in the mixed gas measurement. The measured permeances of He and CO₂ from the pure gas and mixed gas experiments are compared in Figure 2-19. The pure and mixed gas CO₂ permeances are very similar over the entire temperature range. The pure He permeance does not show a significant increase with temperature, and is in good agreement with the plateau of the mixed gas He permeance.

The presence of CO₂ clearly reduces the He permeance at relatively low temperature, when CO₂ adsorption is expected to be significant. It is plausible that the He permeance is reduced due to a reduction in the effective pore radius for Knudsen flow, r_{Kn} . As the membrane temperature increases, r_{Kn} will increase, and at a sufficiently high temperature, r_{Kn} will be equal to the actual

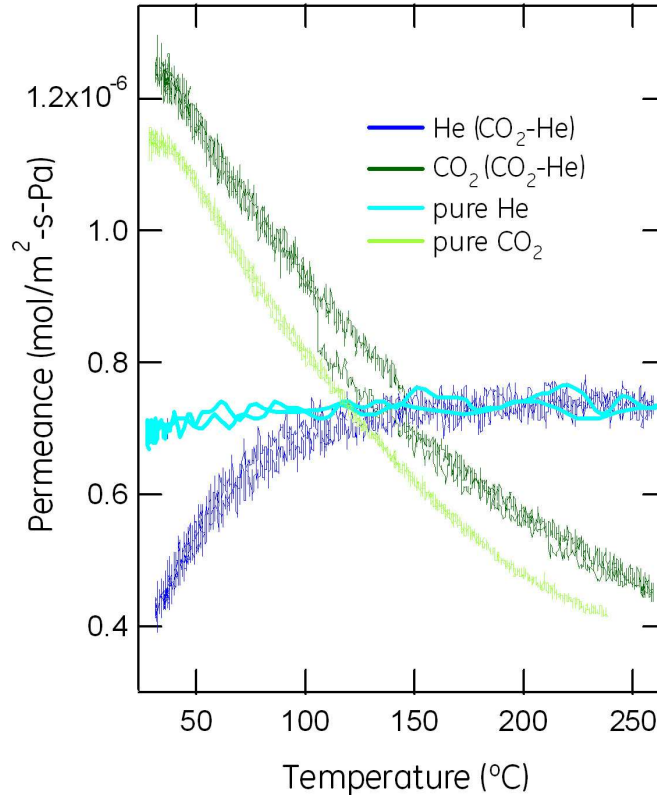


Figure 2-19. Comparison of the permeance of pure He (light blue) and pure CO₂ (light green) to the permeance of He (dark blue) and CO₂ (dark green) from an equimolar He-CO₂ feed

pore diameter, r . By reducing the He flow, the pore blocking effect leads to an increase in CO₂ selectivity. Since the He and H₂ have the same transport behavior, the pore blocking arguments apply equally to the H₂-CO₂ case. From Eq.2-1, $Q_{Kn} \propto \frac{r_{Kn}^3}{\sqrt{T}}$. The ratio of the H₂ permeance at 250 °C to H₂ permeance at 33 °C is equal to 1.58, from the plot in Figure 2-17. Accounting for the temperature dependence of Q_{Kn} , r_{Kn} increases by a factor of 1.27, when the temperature is raised from 33 °C to 250 °C.

The predicted selectivity curves in Figure 2-15 were based on calculated flow through a single pore, for a range of pore radii, and the same ΔP as the experiments. In Figure 2-20, the measured CO₂/H₂ selectivity plot from Figure 2-17 is superimposed on the calculated selectivity curves. Based on the match between model and measured selectivities, the membrane selectivity as a function of temperature is consistent with an increasing average pore radius from 0.9 nm at room temperature to 1.2 nm above to 1.3 nm at 250 °C. Since the selectivity data are reproducible over multiple heating cycles, loss of selectivity due to sample degradation and irreversible microstructural change is ruled out.

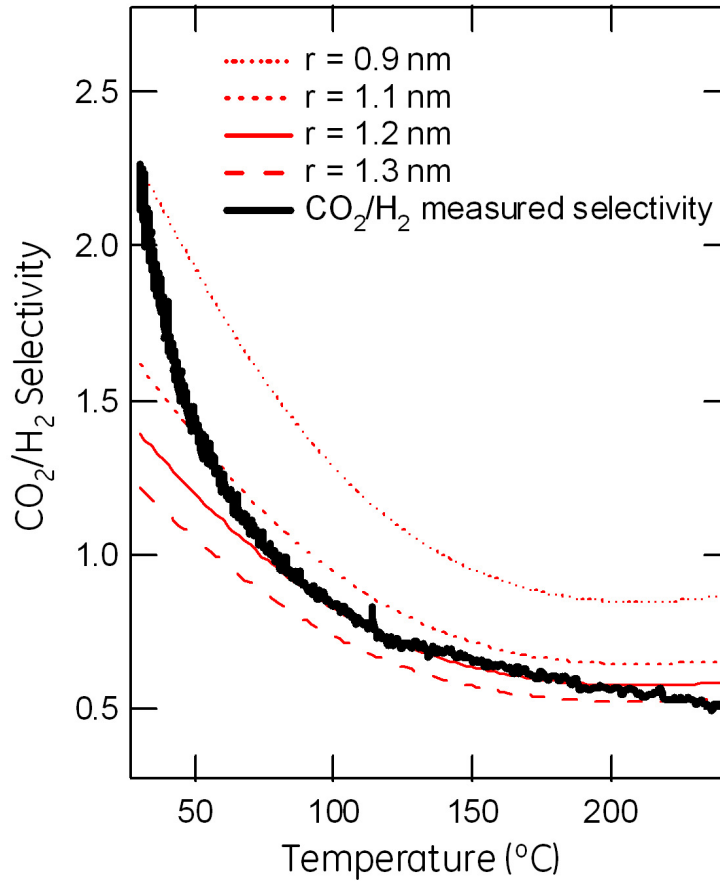


Figure 2-20. Comparison of model predictions (red curves) and measurement (black curve) of CO₂/H₂ selectivity.

The analysis resulting in Eq. 2-10 assumes the same pore radius for Knudsen flow and surface flow. This radius is denoted the effective radius and can be expressed as $r_{eff} = \sqrt{r_{Kn}^3/r_{act}}$, where r_{Kn} is the temperature-dependent Knudsen radius and r_{act} is the actual pore radius. At sufficiently high temperatures, the CO₂ adsorption becomes small, and $r_{Kn} = r_{act}$. Since the CO₂ coverage varies along the pore length, both r_{Kn} and r_{eff} are averaged over the pore length.

By applying Eq. 2-10 to the measured CO₂ selectivity data Figure 2-17, r_{eff} of the membrane was obtained, and r_{Kn} was calculated assuming $r_{Kn} = 1.3$ nm. In Figure 2-21, r_{Kn} and r_{Kn} are plotted as functions for temperature. When temperature increases from 25 °C to 250 °C, r_{Kn} increases by a factor of 1.24. This is in strong agreement with the increase in the Knudsen radius calculated from the H₂ permeance plot in Figure 2-17.

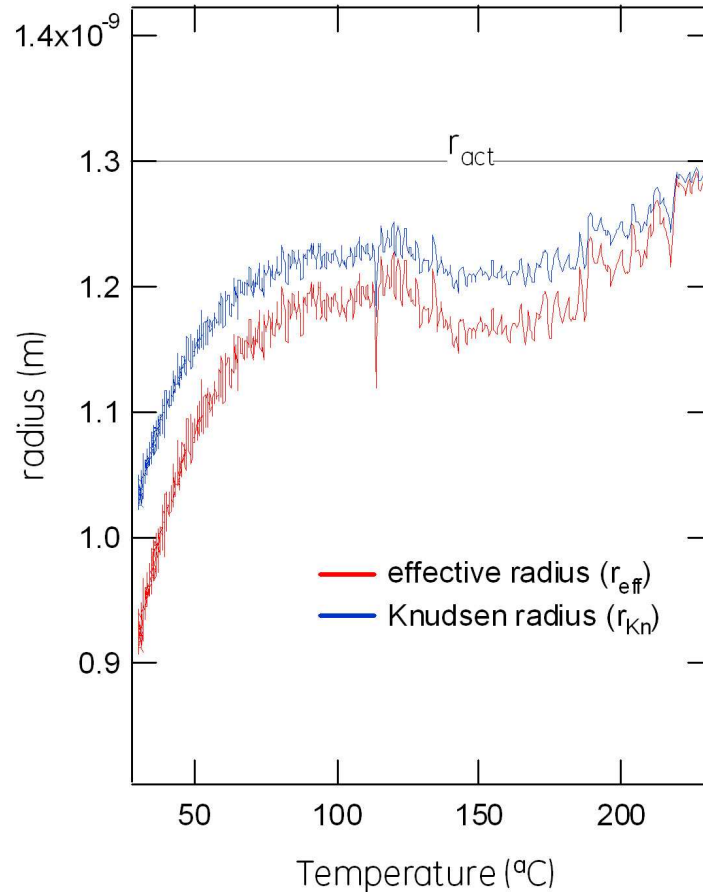


Figure 2-21. Knudsen radius (blue curve - r_{Kn}) and effective radius (red curve - r_{eff}) as a function of temperature.

A model was developed and verified that explicitly predicts the CO₂ selectivity as a function of temperature. Only one fitting parameter, effective pore radius, was used. The model forms the basis of membrane materials design for development of high temperature reverse selective CO₂ membranes.

2.4 MATERIALS SELECTION

Membrane materials for high temperature CO₂ surface transport must have three characteristics: large CO₂ surface concentration at temperature, small heat of adsorption and the ability to be processed with a small pore size. Materials were selected based on the CO₂ adsorption behavior and then subsequently processing methods were evaluated to achieve viscous defect-free membranes with the required pore size. Two approaches were evaluated: functionalization of silica membranes with CO₂ adsorptive materials and processing of barium titanate based membranes. The first approach built on the process development from Section 2.2 that resulted in defect-free silica membranes that achieved room temperature reverse-selectivity, indicating that the required pore structure could be produced. The functionalization of that pore structure was pursued as a way to increase the high temperature selectivity. The second approach was to identify a material with intrinsically high CO₂ adsorption properties and pursue the development of fine pore sizes in that material.

Materials were identified using CO₂ adsorption measurements. When metal oxide surfaces are exposed to CO₂, adsorption takes place by physisorption and chemisorption processes. Chemisorbed CO₂ molecules form monodentate and bidentate surface carbonate species. The surface carbonates can form on metal oxide surfaces even in cases where the metal does not form a stable bulk carbonate phase. That can be rationalized as the result of low coordination of surface atoms and additional configurational degrees of freedom for phase formation. While there is evidence for surface migration of these carbonates on the oxide surfaces [Tsuji, 2003], [Liao, 2002], surface diffusion kinetics have not been extensively quantified. However, near-equilibrium CO₂ adsorption measurements can be used to estimate and compare CO₂ mobility on various oxide surfaces, as outlined below.

In general, the more stable the bulk carbonate, the larger the heat of adsorption of CO₂ and consequently, smaller the surface diffusivities. Alkali and alkaline earth metals form bulk carbonates, and the adsorption of CO₂ on oxides of these metals is characterized by large ΔH on the order of 160 kJ/mol at low surface coverage [Horiuchi, 1998a]. At similar coverage, rare earth oxides have ΔH of about 100-140 kJ/mol [Horiuchi, 1998a]; perovskites have lower ΔH on the order of 50 kJ/mol [Kusakabe, 1994],[Martin, 1981],[Liu, 2005]. Notably, the interaction of CO₂ with basic sites on metal oxides, including perovskites, rare earth oxides and semiconducting oxides, is important in metal oxide-catalyzed reactions such as oxidative coupling of methane, CO₂ reforming of methane, and water gas shift [Tsuji, 2003],[Liu, 2005],[Istadi, 2004]. The catalytic activity of these oxides is consistent with positive but not overly strong surface affinity of CO₂ molecules, since strong CO₂ adsorption would result in poisoning of the active sites. Candidate oxides to be screened for their CO₂ adsorption behavior were selected based on the intermediate ΔH criterion, and include the following:

Families of perovskites: Titanates and Zirconates of Mg, Ca, Sr and Ba;

MgO, CaO, SrO and BaO; (alkaline earth oxides)

CeO₂, La₂O₃ (rare earth oxides)

Al₂O₃, SiO₂ as controls (membrane structure materials)

Published data of CO₂ adsorption properties have been compiled for a variety of metal oxide surfaces, and the CO₂ adsorption behavior of some of these oxides has been characterized in order to validate the measurement capability.

CO₂ adsorption measurements are shown for α -Al₂O₃ and BaTiO₃ powders, using the methods described in Section 2.3. The samples had relative surface areas of 13.58 m²/g and 11.2 m²/g respectively. Isotherms were obtained at temperatures ranging from 100 °C to 500 °C. The sample surfaces were regenerated, between isotherms, by annealing at 600 °C in a He atmosphere to remove remnant adsorbates. These results were benchmarked against adsorption isotherm measurements and analyses have been reported in the literature for γ -Al₂O₃ [Horiuchi, 1998b] and BaTiO₃ [Kusakabe, 1994].

CO₂ adsorption isotherms for α -Al₂O₃ are plotted in Figure 2-22a. The plot shows that CO₂ adsorption decreased with increasing temperature. Adsorption isotherms or lines of constant coverage obtained from the adsorption isotherms in Figure 2-22a are plotted in Arrhenius form (ln P vs. 1/T) in Figure 2-22b. The isotheric heat of adsorption is related to the slopes of the isotherms by the Van't Hoff equation, $\Delta H = -R \frac{d \ln P}{d(1/T)}$. The heat of adsorption as a function of

surface coverage is plotted in Figure 2-23. At low surface coverage the interaction between gas molecules is negligible, and ΔH is dominated by solid-gas interactions. As surface coverage increases there is greater interaction between the CO₂ molecules, and the decrease in ΔH suggests that this interaction is repulsive. CO₂ adsorption isotherms for BaTiO₃ are plotted in Figure 2-24 and the isotheric heat of adsorption is shown in Figure 2-25. Qualitatively, the two materials behave similarly.

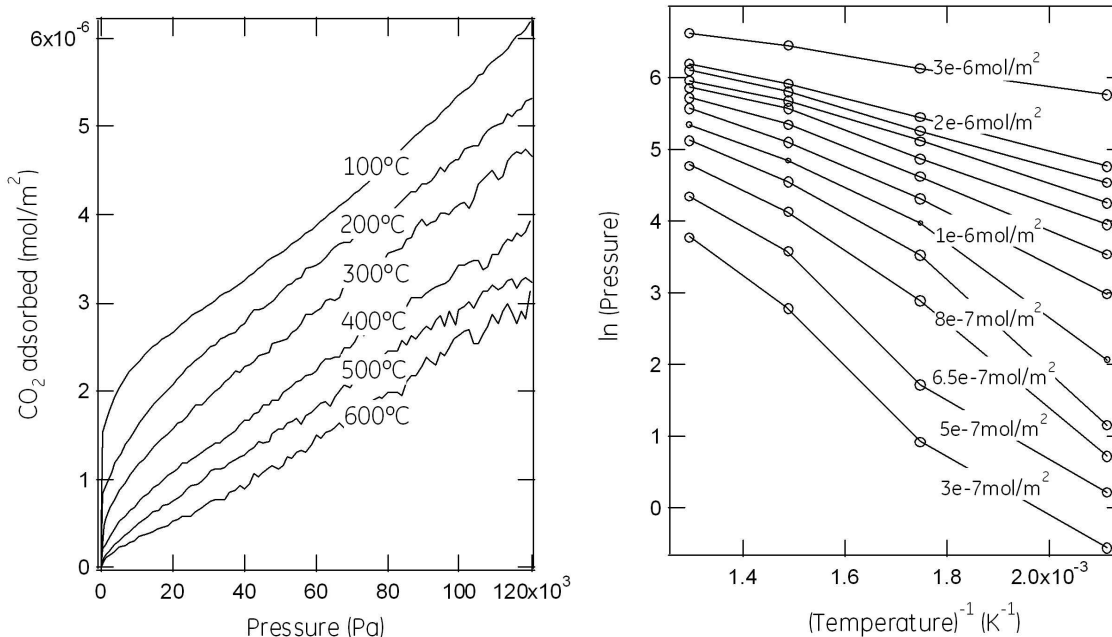


Figure 2-22 a) CO₂ adsorption isotherms for α -Al₂O₃ b) Isotherms for CO₂ for α -Al₂O₃, calculated from adsorption isotherms.

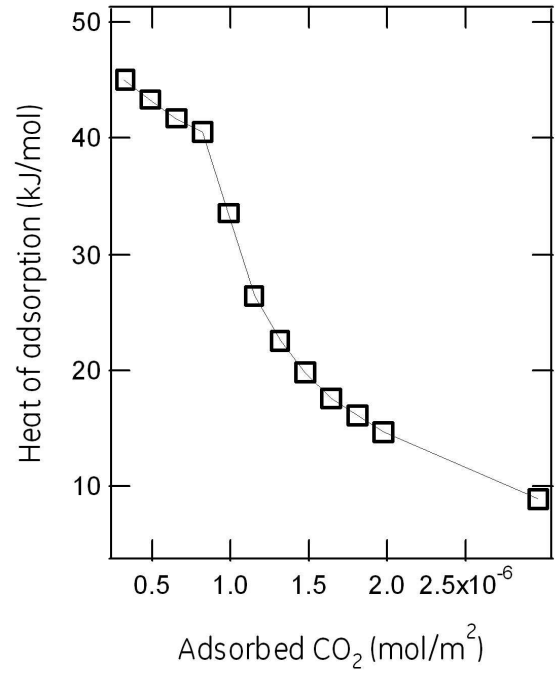


Figure 2-23. Isothermic heat of adsorption as a function of surface coverage for $\alpha\text{-Al}_2\text{O}_3$

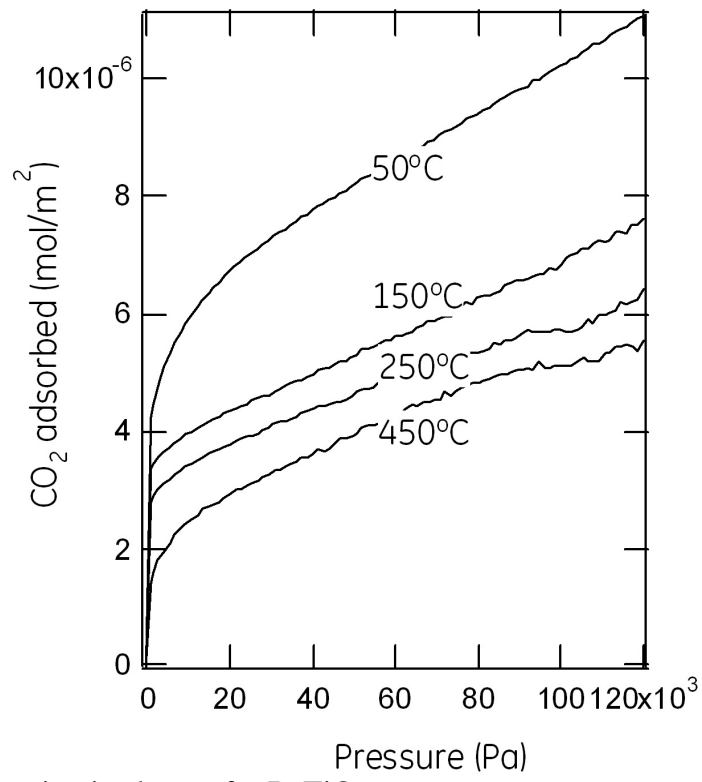


Figure 2-24. CO₂ adsorption isotherms for BaTiO₃

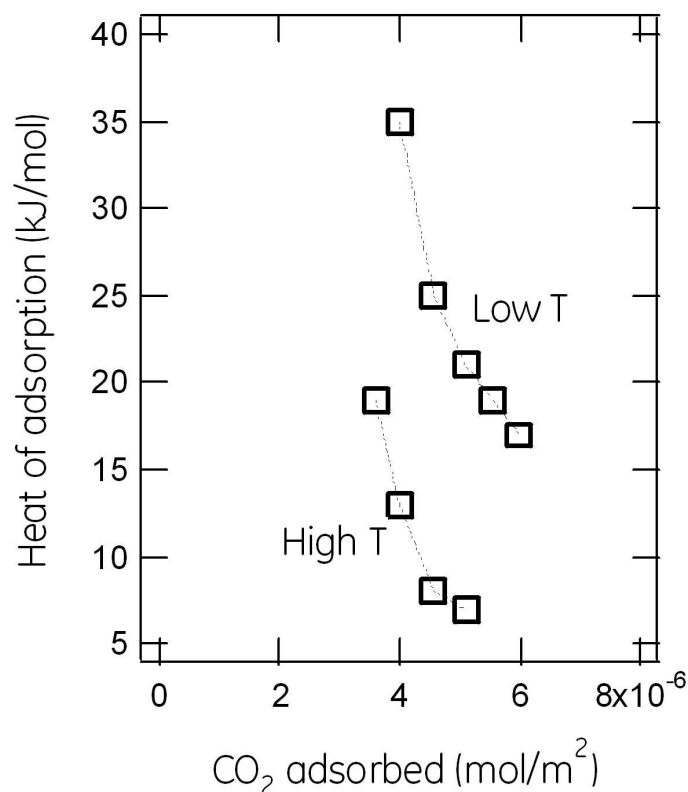


Figure 2-25. Isotheric heat of adsorption for BaTiO₃

Table 2-3. CO₂ adsorption properties for various oxides.

Material	ΔH (kJ/mol)	c_0 ($\mu\text{mol}/\text{m}^2$)	T ($^{\circ}\text{C}$)	Pressure (kPa)	Reference
SiO ₂	20	0.05	250	100	This work
BaTiO ₃	20	6.2	250	100	This work
SrTiO ₃	35	6.1	250	100	This work
α -Al ₂ O ₃	40	4.8	250	100	This work
γ -Al ₂ O ₃	40	0.4	250	100	Horiuchi, 1998
BaTiO ₃	17	4	200	40	Kusakabe, 1994
LaFeO ₃	25	4.4	206	33.3	Martin, 1981
Ba-ZrO ₂	8	3.8	200	100	Liu, 2005
SiO ₂	22	0.03	200	100	DeLange, 1995

Table 2-3 gives a list of CO₂ adsorption properties for oxides. Figure 2-26 shows a set of constraint lines plotted as a function of c_0 vs. ΔH for constant pore size, such that points on or above the lines will have a CO₂/H₂ selectivity of 60 or higher. Markers represent the adsorption properties of various metal oxides, including measurements for α -Al₂O₃ and BaTiO₃. The measured heats of adsorption for both α -Al₂O₃ and BaTiO₃ are in good agreement with values reported in the literature. In the case of BaTiO₃, the c_0 values are also in good agreement. Our

measurements of c_0 for α - Al_2O_3 are much larger than the value reported by Horiuchi [Horiuchi, 1998b]. This difference may be due to the difference in uptake between α - Al_2O_3 (this work) and γ - Al_2O_3 . The properties of BaTiO_3 place it above constraint line for 1 nm diameter pores, making it a promising candidate for membrane functionalization. Of the other oxides, LaFeO_3 [Martin, 1981] lies above the 2 nm diameter constraint line, and Ba-modified ZrO_2 [Liu, 2005] lies above the 4 nm line.

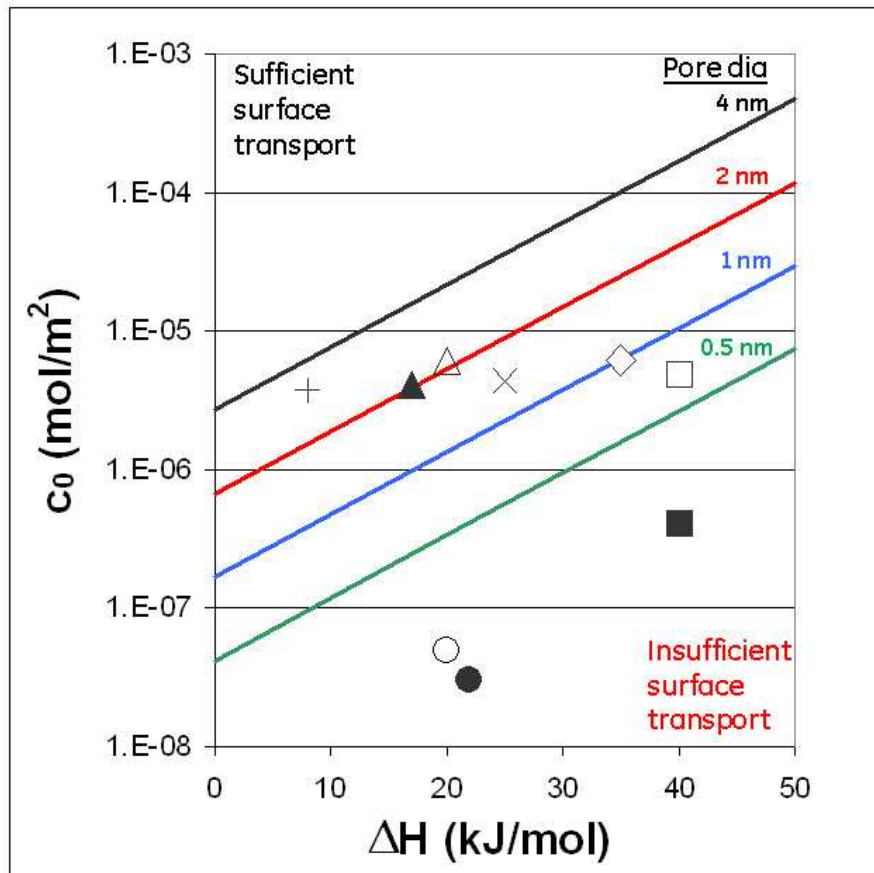


Figure 2-26. Constraint lines on a plot of c_0 versus ΔH plotted for constant pore radius. For each pore size, points defined by c_0 and ΔH on or above the constraint lines show a CO_2/H_2 selectivity of 60 or more at 250 °C. Markers represent the adsorption properties of various oxides with open symbols the results of this work: SiO_2 (circles) [deLange, 1995], BaTiO_3 (triangles) [Kusabe, 1994], Al_2O_3 (squares) [Horiuchi, 1998b], SrTiO_3 (diamond), LaFeO_3 (x) [Martin, 1981], and Ba-ZrO₂ (cross) [Liu, 2005].

2.5 SYNTHESIS OF FUNCTIONALIZED MESOPOROUS MEMBRANES

While silica membranes have the required pore size for reverse-selectivity at room temperature, silica does not have the required CO₂ adsorption at high temperature to permit CO₂ selectivity. Functionalization of the porous silica membrane was selected as a potential way to enhance the selectivity of the membrane at high temperature. In order to achieve high CO₂ selectivity the dopant must be incorporated into the pore wall of the surface area utilized for CO₂ transport. Dopant cations were chosen based on adsorption data and their tendency to form basic oxide materials. Horiuchi et al. [Horiuchi, 1998a] measured retention time of CO₂ on oxide-modified aluminas. Rare earth oxides, alkali metal oxides and alkaline-earth oxides were all shown to increase the retention time of CO₂. CO₂ adsorption was shown to increase for zirconia powders modified with barium oxide and magnesium oxide [Liu, 2005]. In the case of CO₂ separation by surface transport it has been shown in literature that strong basic oxides have an affinity for CO₂ molecules, silica membranes incorporating these dopants have not been fabricated to date. Three dopant cations were selected for study: the two alkaline earth elements Mg and Sr and one rare-earth element La. Horiuchi, et al. [Horiuchi, 1998a] observed that those elements increased the CO₂ retention on alumina in the order Sr>La>Mg.

In this study CO₂/H₂ gas separation testing was performed on silica microporous membranes doped with various concentrations of Mg, La, and Sr. The dopant concentrations were varied from 1 to 25 mol%. In this experiment the salt-based cations were mixed into the aqueous HCl solution to dope the baseline silica recipe. The HCl solution was then added to the TPABr-ETOH solution mixed for ten minutes and then added to the TEOS-ETOH solution. The solution was allowed to mix for twelve hours and stored at 3 °C to prevent premature aging.

In order to control the thickness of the films an aging study was performed. This study was performed at 75 °C over a period of four hours. The results of this study for the solutions doped at 5 and 25 mol% can be seen in Figure 2-27. From this study it was found that the addition of dopants enhances the effects of aging on the microstructure. In order to produce defect free films a target particle size of 10 nm was used to prepare the films for testing.

Scanning electron microscopy images of silica membranes doped with Mg, La and Sr are shown in Figure 2-28, Figure 2-29 and Figure 2-30, respectively. Crack-free membranes were produced with thicknesses in the range of 100-800 nm. The microstructure of the doped membranes was distinctly different from the baseline silica membranes in that platelet shaped voids of less than 100 nm diameter were observed in all the doped membranes.

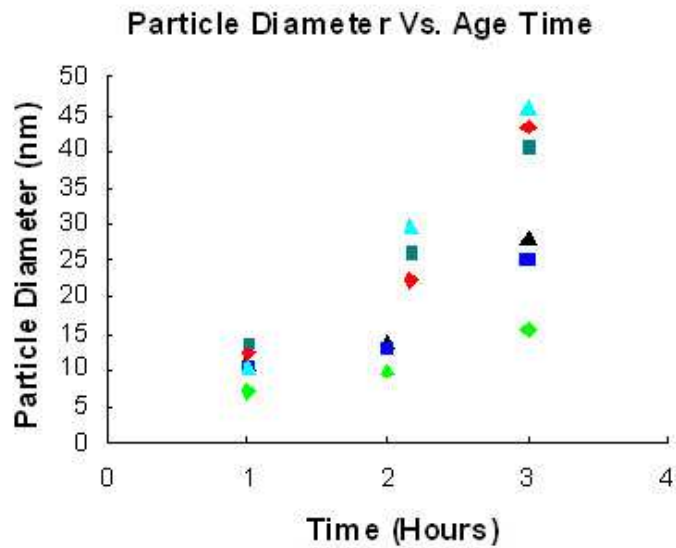


Figure 2-27. Particle diameter as a function of sol age time at 75 °C for doped silica sols with 5 mol% Mg (black triangle), 25 mol% Mg (blue triangle), 5 mol% La (blue square), 25 mol% La (green square), 5 mol% Sr (green diamond) and 25 mol% Sr (red diamond).

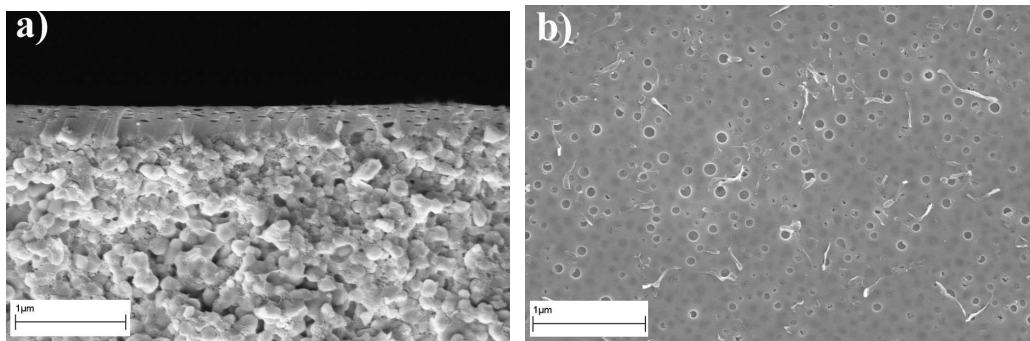


Figure 2-28. a) Cross-section and b) plan view SEM images of 5 mol% Mg doped silica membranes.

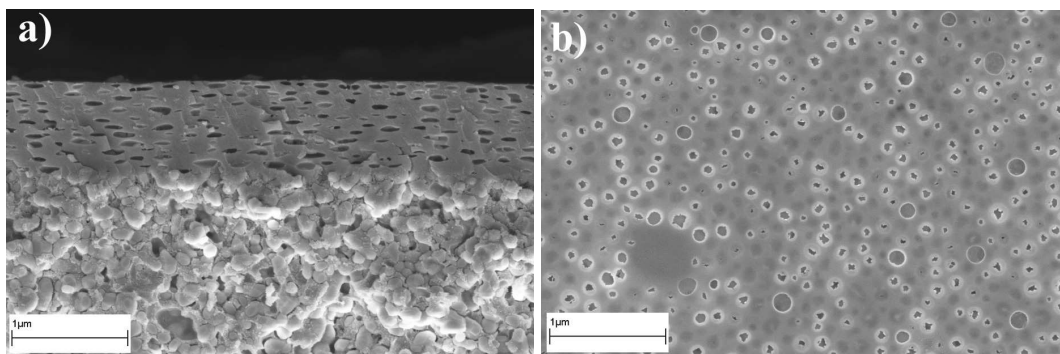


Figure 2-29. a) Cross-section and b) plan view SEM images of 5 mol% La doped silica membranes.

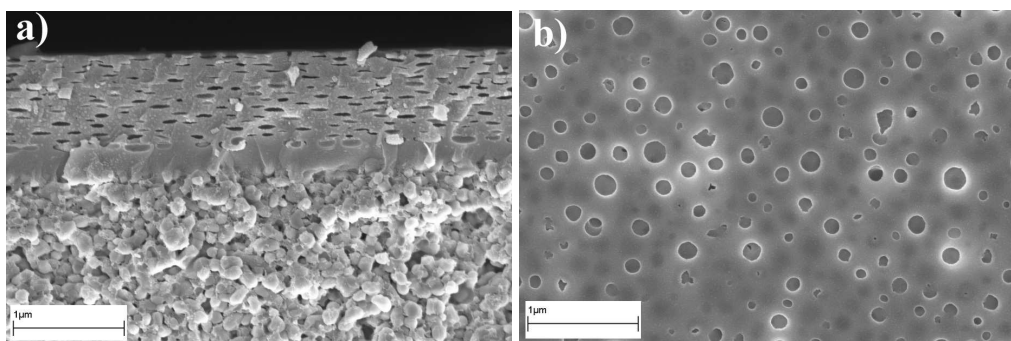


Figure 2-30. a) Cross-section and b) plan view SEM images of 5 mol% Sr doped silica membranes.

Measurements of CO₂/H₂ separation were performed at room temperature for 5 mol% and 25 mol% doped silica membranes as shown in Table 2-4. The 5 mol% doped membranes showed similar separation behavior to the baseline silica membranes, with no enhancement observed. The 25 mol% doped membranes showed a reduced selectivity which was likely to an increase in the concentration of Knudsen defects. The heating profiles of the 5 mol% doped membranes are shown in Figure 2-32 and compared with three of the baseline silica membranes. No evidence of enhanced CO₂ transport at elevated temperatures was observed.

The distribution of the dopant element within the silica membrane was evaluated using Auger Electron Spectroscopy. A relative concentration map of the distribution of Si and Sr on the surface of the membrane is given in Figure 2-31. It appears that the dopant The Auger map indicates that there was significant Sr segregation in the films. This can be a viable reason for a decrease in the selectivity properties of the films as a function of dopant concentration.

Table 2-4. Measurements of CO₂ and H₂ transport through baseline silica and doped silica membranes at room temperature.

	CO ₂ Permeance (mol/m ² s Pa)	H ₂ Permeance (mol/m ² s Pa)	CO ₂ /H ₂ Selectivity
Baseline silica	7.0 x 10 ⁻⁷	2.3 x 10 ⁻⁷	3.0
Mg – 5 mol%	6.4 x 10 ⁻⁷	3.0 x 10 ⁻⁷	2.1
Mg – 25 mol%	1.1 x 10 ⁻⁷	4.0 x 10 ⁻⁷	0.3
La – 5 mol%	3.4 x 10 ⁻⁷	1.7 x 10 ⁻⁷	2.0
La – 25 mol%	6.8 x 10 ⁻⁷	2.6 x 10 ⁻⁶	0.3
Sr – 5 mol%	1.0 x 10 ⁻⁶	4.4 x 10 ⁻⁷	2.3
Sr – 25 mol%	5.2 x 10 ⁻⁹	7.1 x 10 ⁻⁹	0.7

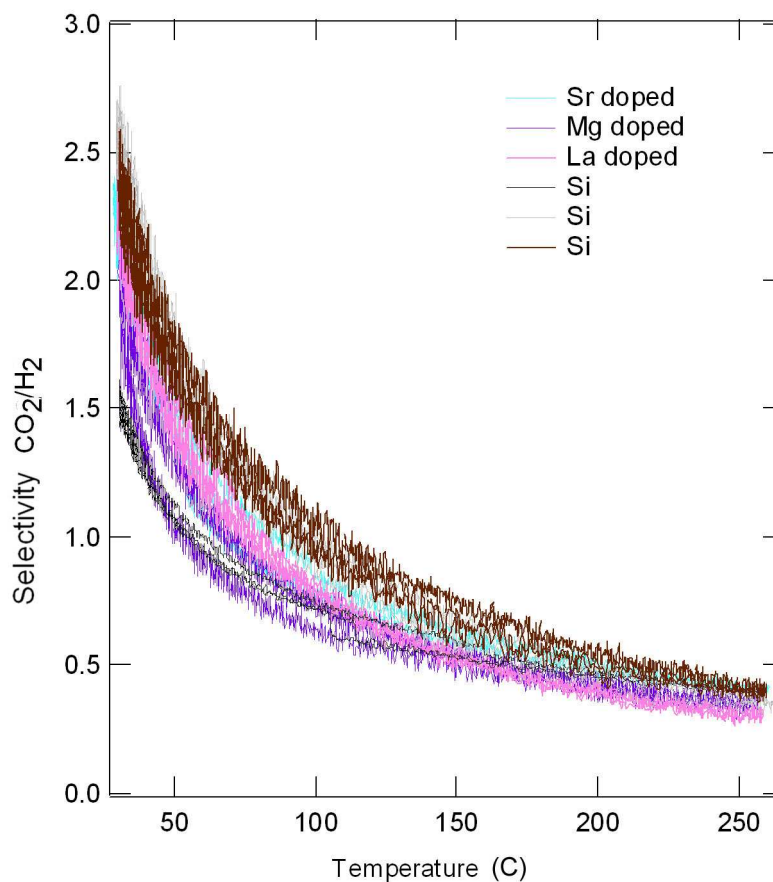


Figure 2-31. CO₂/H₂ selectivity as a function of temperature for 3 silica membranes and for a 5 mol% Sr doped silica (light blue), 5 mol% Mg doped silica (purple) and 5 mol% La doped silica (pink). No significant difference in the high temperature CO₂ transport behavior was observed.

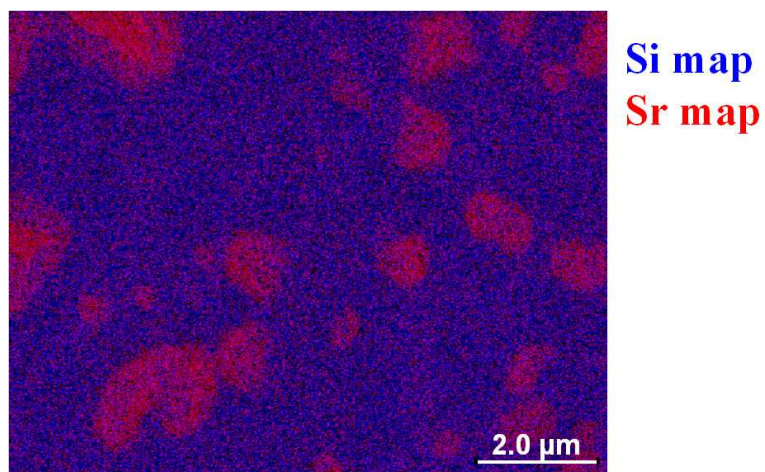


Figure 2-32. Auger elemental mapping of Sr location in a sample doped with 25mol% Sr

2.6 SYNTHESIS OF BARIUM TITANATE BASED MEMBRANES

Barium titanate was selected as a material choice due to its CO₂ adsorption characteristics. A sol gel method utilizing barium acetate and titanium isopropoxide precursor materials was developed consisting of the following molar ratio 1:1:15.76:29.06 Ba(C₂H₃O₂):[(CH₃)₂CHO]₄Ti:CH₃COOH:C₂H₅OH. Defect free films were processed from the spun-coat precursor fired at 400 °C, 550 °C, 600 °C, and 650 °C. X-ray diffraction patterns have shown that BaTiO₃ crystallization does not occur in samples fired at 550-600 °C, crystallization does however occur somewhere between 600 and 650°C. The samples fired at 550°C and 600°C are composed of primarily BaCO₃ and amorphous TiO_x.

The precursor solution for the BaTiO₃ is a combination of a two-part solution. Solution A was made by heating 22.50 g glacial acetic acid to 60 °C, under reflux, in an oil bath. After the solution reached 60 °C 4.515g barium acetate was added to the solution and it was removed from the oil bath. The solution was allowed to mix thoroughly for one hour while cooling to room temperature. Solution B was prepared by adding 5.035 g titanium isopropoxide to 17.95g of ethanol under stirring conditions. It is important that the solutions be mixed at room temperature prevent premature aging. Titanium isopropoxide was added using a dropper over a ten-minute period to insure uniform mixing. The solution was allowed to mix for forty five minutes. The two solutions were combined by adding solution A directly to solution B and they were mixed in a closed container for twelve hours before using.

It was found that to achieve an overlayer of the solution in the desired number of coatings it had to be aged for five days. Aging for five days allowed a 50 nm overlayer to be formed through deposition of four layers through the spin coating process utilizing the same parameters as used for the silica films. Five coats of solution aged for three days gave a 30 nm film as compared to 100nm for the sol aged for five days. The profile for thickness as a function of the number of coatings can be seen in Figure 2-33 for the solution aged for five days, and micrographs of the cross-sections can be seen in Figure 2-34 and Figure 2-35 for samples heated to 550 °C and 650 °C, respectively.

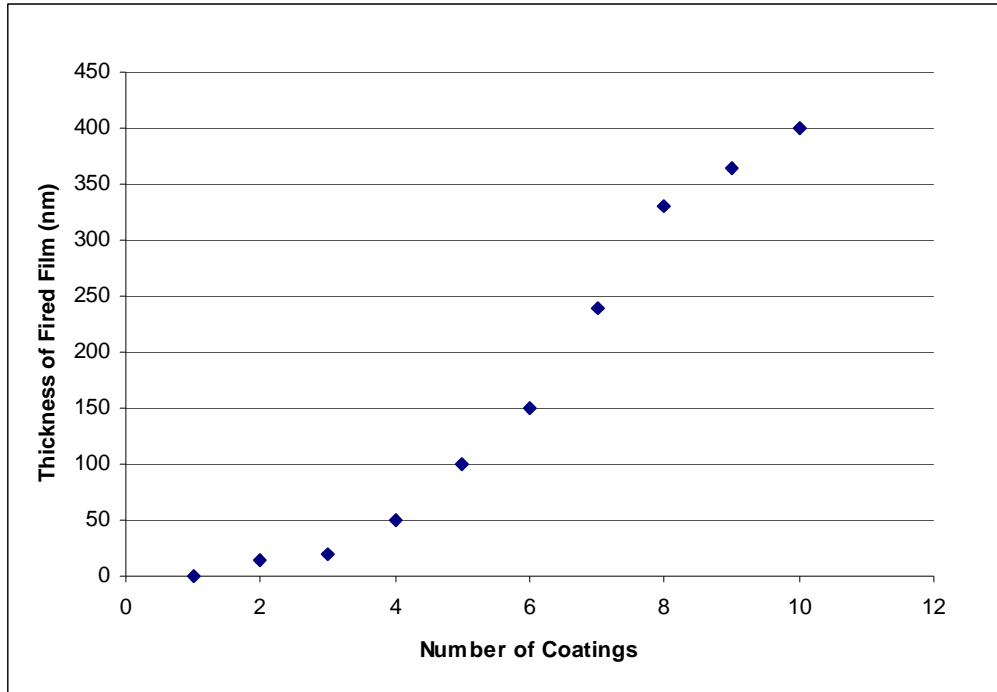


Figure 2-33. Thickness as a function of the number of coatings for barium titanate sol aged five days in a sealed container at room temperature.

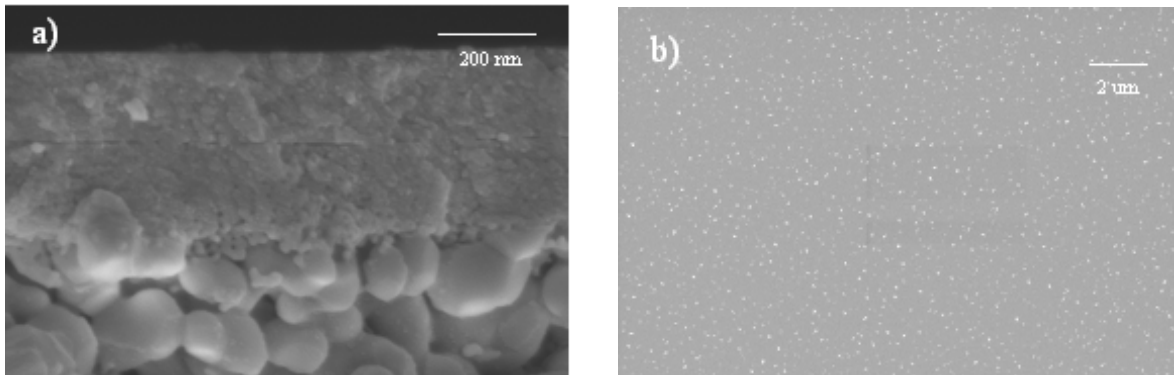


Figure 2-34. Membranes free of viscous defects from barium titanate based sol-gel as BaCO_3 fired at 550°C . a) cross-section b) plan view.

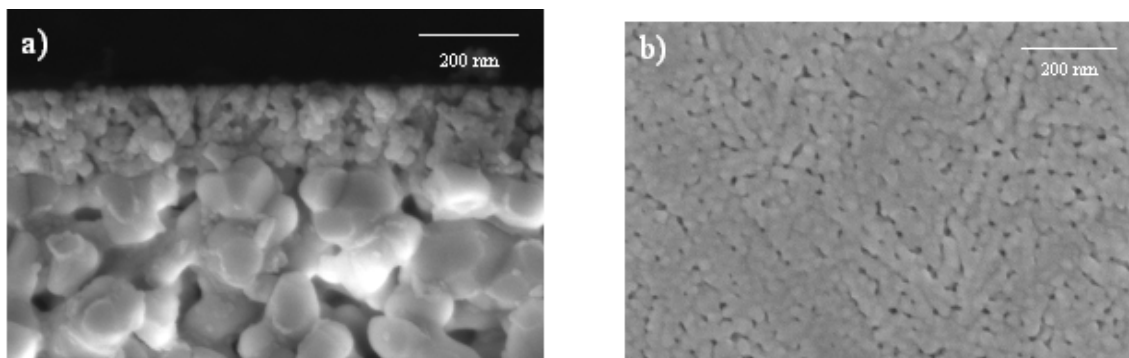


Figure 2-35. Membranes free of viscous defects from barium titanate based sol-gel as BaTiO₃ fired at 650 °C. a) cross-section b) plan view.

The viscous defect-free membranes fired at temperatures at 550 °C were not single phase BaTiO₃ but contained predominantly BaCO₃. Membrane measurements of CO₂/H₂ selectivity at room temperature indicated Knudsen flow was dominant. Samples that were heated to 650 °C were predominantly BaTiO₃ but upon crystallization, the membranes produced large pores that also allowed predominantly Knudsen flow. A set of membranes fired to 400 °C was produced in order to attempt to achieve an amorphous BaTiO₃ network analogous to the silica network that had produced room temperature reverse selectivity. The membranes were free of viscous defects, but only showed a small increase over Knudsen flow at room temperature as shown in Table 2-5.

Table 2-5. CO₂ and H₂ fluxes through best barium-titanate-sol derived membrane.

	CO ₂ Permeance (mol/m ² s Pa)	H ₂ Permeance (mol/m ² s Pa)	CO ₂ /H ₂ Selectivity
Barium-titanate sol at 400 °C	4.8 x 10 ⁻⁷	1.6 x 10 ⁻⁷	0.3

2.7 CONCLUSIONS

A quantitative model was developed and validated for the design of membrane materials capable of high temperature CO₂ reverse selectivity. The model describes porous membranes in which selectivity is endowed through the mechanism of preferential adsorption and surface diffusion of CO₂ along the pore walls. Selectivity for CO₂ over H₂ requires that the surface flow of CO₂ is large compared with the Knudsen flow of H₂ through the bulk of the pore. Selectivity can result from the combination of two mechanisms: enhanced CO₂ surface transport and hindered H₂ transport. Three key membrane design parameters were identified: surface concentration of CO₂, heat of adsorption of CO₂ and effective pore radius. The first two parameters are intrinsic materials parameters that describe the rate of surface diffusion of CO₂. They were measured from chemisorption measurements on oxide powders. The third parameter is a microstructural parameter which accounts for the competitive Knudsen flux of H₂ and for the extent of hindered H₂ flux from pore blocking.

Silica membranes were developed that were free of viscous defects and which had an effective pore radius of less than 1 nm. Those membranes showed reverse selectivity for CO₂/H₂ at room temperature. The selectivity decreased with increasing temperature due to the decrease in surface concentration of CO₂. That caused two effects: the surface transport rate for CO₂ decreased and the H₂ Knudsen flow rate increased as the effective pore size increased. Good quantitative validation was obtained for the predicted selectivity with temperature using the measured chemisorption parameters and only one fitting parameter for the effective pore radius.

On the basis of the model, membrane design parameters were established for the membrane parameters that would allow the attainment of system level separation targets. For pore size diameters of 1-2 nm, heat of adsorption of less than 25 kJ/mol and CO₂ surface concentrations greater than 2 μmol/cm² are required. Materials were screened based on measured adsorption isotherms and those obtained from the literature, with three materials identified as promising candidates.

Two approaches were pursued to synthesize membranes with both the required effective pore size and CO₂ adsorption characteristics. First, silica membranes with the required pore size were functionalized with alkaline and rare earth oxides in order to increase the surface adsorption of CO₂. Second, synthesis of barium titanate based membranes was pursued in order to obtain the required pore size in a material determined to have the required CO₂ surface affinity.

The functionalized silica membranes were produced without viscous defects but no increase in the high temperature CO₂ reverse selectivity over the baseline materials was observed. That may have been due to an inhomogeneous distribution of the functional groups within the membrane or due to a limitation in the concentration attained.

A series of barium-titanate-based membranes was produced that were free of viscous defects, but high temperature reverse selectivity was observed. For the membrane processing temperatures required to produce pure barium titanate, the effective pore size was too large to observe reverse selectivity. At lower processing temperatures, there was a barium carbonate phase present. Only a small increase in CO₂ selectivity over the Knudsen value at room temperature was observed.

Future work for developing reverse-selective CO₂ membranes should focus on developing new processing methods for control of pore size in the materials identified by modeling to be promising candidates. In addition, the materials screening methodology can be applied to identify additional materials that are more amenable to membrane processing in the desired pore size range.

REFERENCES

- Bredesen, R., Jordal, K., and O. Bolland, Chem. Engng. Proc. **43**, 1129-1158 (2004)
- Brinker, C. J.; Scherer, G. W. *Sol-gel Science*. Academic Press, (1990)
- Chiesa, P., Consonni, S., Kreutz, T., and Williams, R., Int. J. Hyd. Energy, **30**, 747-767 (2005)
- Gilliland, E.R., Baddour, R.F., Perkinson, G.P. and K.J. Sladek, Ind. Eng. Chem. Fundam. **13**, 95-100 (1974)
- Gray, D. and Tomlinson, G., "Hydrogen from Coal," Mitretek Technical Paper MTR 2002-31, US DOE NETL, Contract #DE-AM26-99FT40465, (2002)
- Horiuchi, T., Hidaka, H., Fukui, T., Kubo, Y., Horio, M., Suzuki, K., Mori, T., Applied Catalysis A: General, **167**, 195-202 (1998a)
- Horiuchi, T.; Osaki, T.; Sugiyama, T.; Suzuki, K.; Mori, T. J. Coll. Int. Sci., **204**, 217-218 (1998b).
- Huang, J., El-Azzami, L., Ho, W.S.W., J. Membr. Sci. **261**, 67-75 (2005).
- Istadi, Amin, A.A.S., J. Natural Gas Chem., **13**, 23-35 (2004)
- Keizer, K., Uhlhorn, R.J.R. van Vuren, R.J. and A.J. Burggraaf, J. Membrane Sci. **39**, 285-300 (1988).
- Kreutz, T. Williams, R. Consonni, S. and Chiesa, P. Int. J. Hyd. Energy **30**, 769-784 (2005)
- Kusakabe, K., Ichiki, K., Morooka, S., J. Mem. Science **95**, 171-177 (1994)
- de Lange, R.S.A., Keizer, K. and A.J. Burggraaf, J. Membrane Sci. **104**, 81-100 (1995).
- Liao, L.-F., Lien, C.-F., Shieh, D.-L., Chen, M.-T., Lin, J.-L., J. Phys. Chem. B **106**, 11240-11245 (2002)
- Lin, J. S. *Sep. Pur. Tech.* **25**, 39-55 (2003)
- Liu, A., Nyavor, K., and Ankumah, R., J. Colloid and Interface Sci. **284**, 66-70 (2005)
- Martin, M.A., Garcia Fierro, J.L., Gonzalez Tejuca, L., Zeitschrift fur Phys. Chem. Neue Folge **127**, 237-249 (1981)
- Moon, J.-H.; Ahn, H.; Hyun, S.-H.; Lee, C.-H., Korean J. Chem. Eng. **21**, 477-487 (2004)

NETL publication, Texaco Gasifier IGCC Base Cases PED-IGCC-98-001, (2000)

Rao, M.B and S. Sircar, *J. Membrane Sci.* **85**, 253-264 (1993)

Rao, M.B and S. Sircar, *J. Membrane Sci.* **110**, 109-118 (1996)

Shekhawat, D., Luebke, D.R., and Pennline, H.W., "A review of carbon dioxide separation membranes," DOE/NETL-2003/1200 (2003)

Sladek, K. J.; Gilliland, E. R.; Baddour, R. F. *Ind. Eng. Chem. Fundam.*, **13**, 100-105 (1974)

Sloot, H.J., Smolders, C.A., van Swaaij, W.P.M. and G.F. Versteeg, *J. Membrane Sci.* **74**, 263-278 (1992)

Tsuji, H., Okamura-Yoshida, A., Shishido, T., Hattori, H., *Langmuir*, **19**, 8793-8800 (2003)

LIST OF FIGURES

Figure 1-1. Process flow diagram of coal-to-hydrogen plant with CO₂ separation

Figure 1-2. CO₂-selective WGS membrane reactor in a coal-to-hydrogen plant

Figure 1-3. Prototype membrane reactor design

Figure 1-4. Membrane reactor model and baseline case two-stage water gas shift model.

Figure 1-5. Gas composition profile in a two-stage water-gas-shift reactor

Figure 1-6. Gas composition profile in a CO₂ membrane water-gas-shift reactor.

Figure 1-7. H₂S composition profile in a CO₂-membrane water-gas-shift reactor.

Figure 2-1. Calculated required adsorption properties for CO₂/H₂ selectivity of 60 at 250 °C as a function of the pore diameter. Materials parameters from the region below the line of constant pore diameter do not provide sufficient surface transport to meet the selectivity target and materials parameters from the region above the line do meet the selectivity target.

Figure 2-2. Percentage weight (green curve) and derivative weight (blue curve) as a function of temperature for silica sol as measured by thermal gravimetric analysis.

Figure 2-3. Viscous flow through the membrane as a function of thickness. Three regions were identified a) defects from incomplete filling, b) viscous defect-free, and c) defects from cracking.

Figure 2-4. Scanning electron micrographs of silica membranes for the three regions identified in Figure 2-3 a) incompletely filled membrane, b) viscous defect-free membrane and c) cracking defect.

Figure 2-5. Thickness of the silica layer as a function of solution aging time for the first coating layer (black triangles) and second coating layer (blue squares).

Figure 2-6. Membrane thickness as a function of solution age for sol aged at room temperature (black triangles) and aged at 55 °C (blue diamonds).

Figure 2-7. Particle diameter as a function of time for sols aged at room temperature (blue squares with time measured in days), sols aged at 55 °C (black triangles with time measured in hours) and sols aged at 75 °C (green triangles with time measured in hours).

Figure 2-8. Membrane thickness as a function of sol particle size for room temperature aged sol (black triangles) and sol aged at 55 °C (blue squares).

Figure 2-9. Schematic of test rig for measurement of room temperature gas separation

Figure 2-10. Histogram of room temperature CO₂/He separation observed for viscous defect-free silica membranes

Figure 2-11. Transmission electron microscopy image of a reverse-selective silica film produced with three sequential coating applications. The porogen had segregated within the layers.

Figure 2-12. CO₂ adsorption isotherms for SiO₂ as a function of pressure.

Figure 2-13. Isoteric heat of adsorption for SiO₂ as a function of adsorbed CO₂ concentration.

Figure 2-14. $c_0/\Delta P$ at 82 Pa, calculated from the CO₂ adsorption isotherms

Figure 2-15. CO₂/H₂ selectivity predictions as function of temperature, for pore radii ranging from 0.9 nm to 1.3 nm.

Figure 2-16. Membrane separation test rig

Figure 2-17. CO₂-H₂ (CO₂ permeance in dark green and H₂ permeance in red) and CO₂-He (CO₂ permeance in light green and He permeance in blue) separation performance of SiO₂ membrane.

Figure 2-18. CO₂ selectivity as function of temperature for CO₂-H₂ (black curve), CO₂-He (gray curve) and CO₂-H₂ predicted from scaling CO₂-He data by Knudsen diffusion differences (red curve)

Figure 2-19. Comparison of the permeance of pure He and pure CO₂ to the permeance of He and CO₂ from an equimolar He-CO₂ feed

Figure 2-20. Comparison of model predictions (red curves) and measurement (black curve) of CO₂/H₂ selectivity.

Figure 2-21. Knudsen radius (blue curve - r_{Kn}) and effective radius (red curve - r_{Kn}) as a function of temperature.

Figure 2-22 a) CO₂ adsorption isotherms for α -Al₂O₃ b). Isoteres for CO₂ for α -Al₂O₃, calculated from adsorption isotherms.

Figure 2-23. Isoteric heat of adsorption as a function of surface coverage for α -Al₂O₃

Figure 2-24. CO₂ adsorption isotherms for BaTiO₃

Figure 2-25. Isoteric heat of adsorption for BaTiO₃

Figure 2-26. Constraint lines on a plot of c_0 versus ΔH plotted for constant pore radius. For each pore size, points defined by c_0 and ΔH on or above the constraint lines show a CO₂/H₂ selectivity

of 60 or more at 250 °C. Markers represent the adsorption properties of various oxides with open symbols the results of this work: SiO₂ (circles) [deLange, 1995], BaTiO₃ (triangles) [Kusabe, 1994], Al₂O₃ (squares) [Horiuchi, 1998b], SrTiO₃ (diamond), LaFeO₃ (x) [Martin, 1981], and Ba-ZrO₂ (cross) [Liu, 2005].

Figure 2-27. Particle diameter as a function of sol age time at 75 °C for doped silica sols with 5 mol% Mg (black triangle), 25 mol% Mg (blue triangle), 5 mol% La (blue square), 25 mol% La (green square), 5 mol% Sr (green diamond) and 25 mol% Sr (red diamond).

Figure 2-28. a) Cross-section and b) plan view SEM images of 5 mol% Mg doped silica membranes.

Figure 2-29. a) Cross-section and b) plan view SEM images of 5 mol% La doped silica membranes.

Figure 2-30. a) Cross-section and b) plan view SEM images of 5 mol% Sr doped silica membranes.

Figure 2-31. CO₂/H₂ selectivity as a function of temperature for 3 silica membranes and for a 5 mol% Sr doped silica (light blue), 5 mol% Mg doped silica (purple) and 5 mol% La doped silica (pink). No significant difference in the high temperature CO₂ transport behavior was observed.

Figure 2-32. Auger elemental mapping of Sr location in a sample doped with 25mol% Sr

Figure 2-33. Thickness as a function of the number of coatings for barium titanate sol aged five days in a sealed container at room temperature.

Figure 2-34. Membranes free of viscous defects from barium titanate based sol-gel as BaCO₃ fired at 550 °. a) cross-section b) plan view.

Figure 2-35. Membranes free of viscous defects from barium titanate based sol-gel as BaTiO₃ fired at 650 °. a) cross-section b) plan view.

LIST OF TABLES

Table 1-1. Calculated system parameters

Table 2-1. Porogens evaluated for effect on pore structure in silica membranes

Table 2-2. Porogen type, CO₂ permeance, H₂ permeance and CO₂/H₂ selectivity at room temperature

Table 2-4. Measurements of CO₂ and H₂ transport through baseline silica and doped silica membranes at room temperature.

Table 2-5. CO₂ and H₂ fluxes through best barium-titanate-sol derived membrane.

LIST OF ACRONYMS AND ABBREVIATIONS

Acronym	Definition
CAPEX	Capital expenditure
DDABr	Didecyldimethyl-ammonium Bromide
DLS	Dynamic light scattering
EtOH	Ethanol
HHV	Higher heating value
HTS	High temperature shift
IGCC	Integrated gasification combined cycle
LTS	Low temperature shift
MMscfd	Million standard cubic feet per day
MTES	Methyltriethoxysilane
OTES	Octyltriethoxysilane
PSA	Pressure swing adsorption
SEM	Scanning electron microscopy
TMABr	Tetramethylammonium Bromide
TPABr	Tetrapropylammonium Bromide
TPD	Tons per day
WGS	Water gas shift
XRD	X-ray diffraction